

The vertical structure and entrainment of subglacial melt water plumes

Hans Burchard¹, Karsten Bolding², Adrian Jenkins^{3,4}, Martin Losch⁵, Markus Reinert¹, and Lars Umlauf¹

¹Leibniz Institute for Baltic Sea Research Warnemünde, Seestr. 15, D-18119 Rostock, Germany

²Bolding & Bruggeman ApS., Strandgyden 25, DK-5466 Asperup, Denmark

³British Antarctic Survey, Natural Environment Research Council, Cambridge, United Kingdom

⁴Department of Geography and Environmental Sciences, Northumbria University, Newcastle upon Tyne, United Kingdom

⁵Alfred-Wegener-Institut, Helmholtz-Zentrum für Polar- und Meeresforschung, Bremerhaven, Germany

Key Points:

- A vertically resolving model with second-moment turbulence closure has been constructed for subglacial plumes
- Convergent numerical formulations for the ocean-to-ice fluxes of momentum, fresh-water and heat have been derived from an analytical model
- Model results are consistent with bulk parameterizations for the entrainment of ambient water

Corresponding author: Hans Burchard, hans.burchard@io-warnemuende.de

Abstract

Basal melting of marine-terminating glaciers, through its impact on the forces that control the flow of the glaciers, is one of the major factors determining sea level rise in a world of global warming. Detailed quantitative understanding of dynamic and thermodynamic processes in melt-water plumes underneath the ice-ocean interface is essential for calculating the subglacial melt rate. The aim of this study is therefore to develop a numerical model of high spatial and process resolution to consistently reproduce the transports of heat and salt from the ambient water across the plume into the glacial ice. Based on boundary layer relations for momentum and tracers, stationary analytical solutions for the vertical structure of subglacial non-rotational plumes are derived, including entrainment at the plume base. These solutions are used to develop and test convergent numerical formulations for the momentum and tracer fluxes across the ice-ocean interface. After implementation of these formulations into a water-column model coupled to a second-moment turbulence closure model, simulations of a transient rotational subglacial plume are performed. The simulated entrainment rate of ambient water entering the plume at its base is compared to existing entrainment parameterizations based on bulk properties of the plume. A sensitivity study with variations of interfacial slope, interfacial roughness and ambient water temperature reveals substantial performance differences between these bulk formulations. An existing entrainment parameterization based on the Froude number and the Ekman number proves to have the highest predictive skill. Recalibration to subglacial plumes using a variable drag coefficient further improves its performance.

Plain Language Summary

In a world of global warming, the melting of glaciers terminating as floating ice tongues into the oceans of Arctic and Antarctic regions allows those glaciers to flow faster and hence to make a considerable contribution to global mean sea-level rise. Underneath the ice-ocean interface, turbulent currents of the order of 10 m thickness (so-called plumes) develop that transport the melt water from the grounding line where the glacier enters the ocean towards the calving front that marks the seaward end of the glacier. At its base, ambient relatively warm and salty ocean water is mixed into the plumes and is vertically transported towards the ice-ocean interface, where the melting is increased due to the additional heat supply. Understanding these processes is essential for their incorporation into computer simulation models for the prediction of such melt processes. In the present study, an accurate simulation model for the water column (vertical direction only) is constructed that is able to consistently reproduce these processes. The algorithms developed here are proven to provide reliable results also for relatively coarse vertical resolution and can therefore be implemented into climate models to more accurately simulate future scenarios of sea level rise.

1 Introduction

The accelerated melting of Greenland's glaciers contributed to a net global mean sea level rise of 7.5 mm during the years 1992-2011 (Church et al., 2011). Around Greenland, the melt water enters the ocean largely through glacial fjords, mainly as subglacial discharge at the grounding lines of marine-terminating glaciers or as subglacial melt fluxes at the ice-ocean interface (Straneo & Cenedese, 2015). Increased melting at the ice-ocean interface it thought to be responsible for the acceleration of many of Greenland's marine terminating glaciers and thus to have contributed to the sea level rise. Some large Greenland fjords are covered with ice tongues of marine-terminating glaciers such as the Nioghalvfjærdsfjorden, also called 79°N glacier fjord (Mayer et al., 2018), and the Petermann Gletscher (Münchow et al., 2014). For these glaciers the link between submarine

melting and glacier flow is clear, because melt-driven thinning of the floating ice tongue reduces buttressing of the flow across the grounding line (Goldberg et al., 2009).

For the largest floating ice tongue of the 79°N glacier, only 11% of the freshwater enters the fjord directly as subglacial discharge, and about 89% stems from subglacial melting at the ice-ocean interface (Schaffer et al., 2020). Hence, a cold and relatively fresh buoyant water mass composed of contributions from subglacial discharge, melt water and entrained ambient ocean water is produced that propagates upwards towards the calving front as a turbulent plume (Hewitt, 2020). The correct quantification and prediction of the subglacial melt rate under highly variable environmental conditions has been an aim of polar oceanography for decades. Melt processes in the melt layer are typically parameterized based on a three-equation model for melt-layer temperature, melt-layer salinity and melt rate derived from equilibrium fluxes of freshwater and heat across the melt layer (Hellmer & Olbers, 1989). The challenge is to relate these processes to the properties of the underlying subglacial plume. To this end, similarity relations are typically applied, resulting in logarithmic profiles for momentum and tracers in the near-interfacial region of the melt water plume (Kader & Yaglom, 1972; Yaglom & Kader, 1974; Kader, 1981).

After applying the similarity relations for a vertically integrated model of subglacial plumes (Jenkins, 1991, 1992), plume models have become powerful tools for understanding melt processes underneath floating ice tongues and ice shelves (P. R. Holland & Feltham, 2006; Payne et al., 2007; Jenkins et al., 2010; Jenkins, 2011). Their strength is the computational efficiency allowing high horizontal resolution and the reproduction of the plume thickness, but they rely on accurate parameterizations of entrainment of ambient ocean water into the plume. Many different entrainment parameterizations exist (Jungclauss & Backhaus, 1994; Arneborg et al., 2007; Wells et al., 2010). These are generally derived for dense bottom currents and typically depend on non-dimensional bulk parameters such as the bulk Richardson number, the Froude number or the Ekman number. A specifically simple and robust parameterization is based on a constant entrainment rate (ratio of entrainment velocity to plume current speed, Jenkins, 1991). The diversity of entrainment parameterizations shows that there is quite an uncertainty in determining the plume dynamics. In spite of their success, plume models have their specific limitations: They do not predict the ocean temperature and salinity underneath the plume such that the amount of entrained heat and salt is highly uncertain.

To overcome the limitations of plume models and to predict better the effects of larger scale ocean processes, three-dimensional ocean models with explicit ice shelf-ocean interfaces were developed.

For ocean models with geopotential coordinates, a result of the typical step-like approximation of slopes is that the sloping ice-ocean interface is poorly resolved (Losch, 2008). To avoid this issue, terrain-following coordinates are often used where the top layer follows the ice-ocean interface and the lower most layer follows the bottom topography, with non-linear zooming of layers towards surface and bottom (Dinniman et al., 2007). Due to the pressure gradient errors in models with terrain-following coordinates (Haney, 1991), large scale ocean models including ice shelves sometimes apply hybrid coordinates with terrain-following properties inside ice shelves and geopotential coordinates elsewhere (Timmermann et al., 2012). Terrain-following coordinates have the clear advantage of smoothly resolving the ice-ocean interface at high vertical resolution. However, their disadvantage is that the vertical resolution near the ice-ocean interface depends directly on the water depth. Typical top-layer resolutions of terrain-following ice-shelf models around Antarctica vary between 0.5 m near the grounding line and 5 m near the calving front (Gwyther et al., 2020). In models with higher vertical resolution near the ice-ocean interface, the insulating effect of subglacial plumes could be better reproduced than coarse-resolution models (Gwyther et al., 2020). As a consequence, coarse resolution models tend to overestimate melt rates at the ice-ocean interface. Vertically adaptive coordi-

120 nates with specifically high resolution in the entrainment layer (Hofmeister et al., 2010;
121 Gräwe et al., 2015), which would have the potential to resolve subglacial plumes inde-
122 pendently of the water depth, have not yet been used in models with an ice shelf-ocean
123 interface.

124 We can expect that improved strategies for vertical coordinates and available com-
125 puter resources will allow very high vertical resolution of subglacial plumes and grav-
126 ity currents, so that related processes can be simulated more accurately with the prospect
127 of higher predictability of the melt rate. A similar emphasis should be placed on real-
128 istic turbulence closure schemes in circulation models underneath ice shelves, because
129 the basal melt rates strongly depend on the parameterization of mixing processes and
130 entrainment (Dansereau et al., 2014). Exploring these aspects is best to be done with
131 one-dimensional water-column models, because with these, very high vertical resolution
132 can be achieved at little computational cost.

133 Water column models, also with second-moment turbulence closures, have been used
134 to study melting (and freezing) under sea ice (Omstedt & Svensson, 1984; Mellor et al.,
135 1986; Steele et al., 1989). Analogous studies of the vertical structure of subglacial plumes
136 are in their infancy, but include models with simple (Jenkins, 2016, 2021) and two-equation
137 turbulence closures (C. Cheng et al., 2020). In these models, a well-mixed turbulent bound-
138 ary layer is separated from the ambient water underneath by a stratified layer at marginal
139 stability, across which quiescent ambient water is entrained. The resulting profiles of ve-
140 locity and eddy diffusivity are very sensitive to parameters such as the roughness of the
141 ice-ocean interface or the transfer velocities for salt and heat. However, the simplicity
142 of the applied turbulence closures in the former case and the particularity of the appli-
143 cation in the latter case render general applicability of the results very uncertain specif-
144 ically in the region of the entrainment layer. While Direct Numerical Simulation (DNS,
145 Rosevear et al., 2021) and Large Eddy Simulation (LES, Vreugdenhil & Taylor, 2019)
146 have been applied to the ice-shelf-ocean boundary, the entrainment layer has not yet been
147 studied in these applications because of the limited spatial scales considered. In the present
148 study we overcome these limitations and develop, present, and apply a more general high-
149 resolution water-column model for subglacial plumes that includes realistic second-moment
150 turbulence closures.

151 Melt processes under floating ice tongues are very difficult to observe in their harsh
152 and barely accessible polar environments. Therefore, the dynamic analogy between buoy-
153 ant plumes under shelf ice and dense bottom currents due to overflows across sills have
154 been applied to validate plume models (Jenkins, 2016). The main difference is that in
155 ice shelves the buoyancy is mostly produced locally due to subglacial melt, but the (neg-
156 ative) buoyancy in dense bottom currents is a result of upstream processes. While this
157 certainly has substantial effects on larger time and space scales, the vertical structure
158 of both regimes may be comparable. Exploiting this analogy, most formulations for en-
159 trainment in plume models are derived from studies of dense bottom currents. In the
160 present study, we apply previous modeling concepts of simulating rotational dense bot-
161 tom currents in the Western Baltic Sea (Arneborg et al., 2007; Umlauf et al., 2010). The
162 subglacial plume model developed here serves the following purposes:

- 163 1. develop a consistent dynamic coupling between parameterized melt layer processes
164 and turbulent processes within the plume and the entrainment layer,
- 165 2. develop consistent and convergent discretization methods for melt fluxes that give
166 robust results also for relatively coarse resolution, and
- 167 3. test existing formulations and calibrate a new parameterization of entrainment that
168 can be applied in vertically integrated plume models.

169 This paper is structured as follows: First, the underlying mathematical formula-
170 tions are given, with the water-column equations (Sec. 2.1), the boundary conditions (Sec.

2.2), the melt formulations (Sec. 2.3), the tracer roughness lengths (Sec. 2.4), and a stationary analytical model of the vertical plume structure (Sec. 2.5). Afterwards, numerical issues are discussed, with discretization methods for velocity (Sec. 3.1) and tracers (Sec. 3.2), the numerical treatment of the free surface (Sec. 3.3), and with numerical convergence experiments (Sec. 3.4). The transient model simulations with the turbulence closure model are described, with the model setup (Sec. 4.1), the models results including the default scenario and sensitivity studies are presented (Sec. 4.2), and a comparison of the model results to the performance of entrainment parameterizations is made, including calibration of a new formulation (Sec. 4.3). Finally, the main results of the study are discussed (Sec. 5) and some conclusions are drawn (Sec. 6). In the appendix, details of the analytical solution (Sec. Appendix A) and an analytical dependence of plume speed and friction velocity on the interfacial roughness length (Sec. Appendix B) are given.

2 Materials and Methods

2.1 Water-column model equations

The hydrodynamic and hydrographic water column equations for a buoyant melt water plume under a planar ice-ocean interface with slope $\partial_x z_b = \tan \alpha_x$, $\partial_y z_b = \tan \alpha_y$ (with the vertical position of the ice-ocean interface $z = z_b$, where z is the upward directed vertical coordinate with the origin at the undisturbed mean sea level) are based on the Reynolds-averaged Navier-Stokes equations with the Boussinesq assumption and the down-gradient parameterization of vertical turbulent fluxes (Umlauf & Burchard, 2005). We assume that stagnant and homogeneous ambient water with velocities $u = v = 0$, potential temperature $\theta = \theta_0$, salinity $S = S_0$ and potential density $\rho = \rho_0$ below the plume. The z -axis is assumed to be pointing upwards exactly opposite to the gravitational acceleration. The plume properties are assumed to be homogeneous along the ice-ocean interface, i.e. all gradients along the slope vanish:

$$\partial_x = -\tan \alpha_x \cdot \partial_z, \quad \partial_y = -\tan \alpha_y \cdot \partial_z. \quad (1)$$

In a one-dimensional hydrostatic water column model the pressure-gradient driven acceleration in x -direction is calculated as

$$-\frac{1}{\rho_0} \partial_x p = -\frac{1}{\rho_0} \partial_x p(z_b) - \frac{g}{\rho_0} \rho(z_b) \tan \alpha_x - \frac{g}{\rho_0} \int_z^{z_b} \partial_x \rho \, dz', \quad (2)$$

with the surface pressure $p(z_b)$ (from atmospheric pressure plus the additional pressure due to glacial ice). Using (1) we obtain

$$-\frac{1}{\rho_0} \partial_x p = -\frac{1}{\rho_0} \partial_x p(z_b) - \frac{g}{\rho_0} \rho \tan \alpha_x. \quad (3)$$

For the ambient stagnant water below the plume with $z \rightarrow -\infty$ and $\rho(-\infty) = \rho_0$, we demand that the pressure gradient vanishes, i.e.,

$$0 = -\frac{1}{\rho_0} \partial_x p(z_b) - \frac{g}{\rho_0} \rho_0 \tan \alpha_x, \quad (4)$$

such that we obtain

$$-\frac{1}{\rho_0} \partial_x p = -\frac{g}{\rho_0} (\rho - \rho_0) \tan \alpha_x = b \tan \alpha_x \quad (5)$$

with the buoyancy

$$b = -g \frac{\rho - \rho_0}{\rho_0}, \quad (6)$$

which is positive inside the subglacial plume and vanishes in the ambient water. The pressure gradient in y -direction is calculated accordingly, such that the dynamic equations for the velocity components u and v read

$$\begin{aligned} \partial_t u - \partial_z (\nu_t \partial_z u) - f v &= b \tan \alpha_x, \\ \partial_t v - \partial_z (\nu_t \partial_z v) + f u &= b \tan \alpha_y, \end{aligned} \quad (7)$$

with the eddy viscosity ν_t and the Coriolis frequency f . The second terms on the left hand side represents the stress divergence with the stress vector

$$(\tau^x, \tau^y) = \rho_0 \nu_t (\partial_z u, \partial_z v). \quad (8)$$

Similar dynamic equations have been used for simulations of subglacial plumes (Jenkins, 2016, 2021) as well as for dense bottom currents, where less dense ambient water resides above the plume (Arneborg et al., 2007). In both modelling concepts, the coordinate system is defined such that the z -axis is orthogonal to the slope of the model instead of being aligned with the gravitational forcing. However, for mild slopes, the differences to our approach outlined above are negligibly small. In the present study, the formulation of a vertical z -axis is used in order to be consistent with hydrostatic three-dimensional ocean models, which lose their validity for steep slopes where the vertical acceleration becomes relevant.

The budget equations for potential temperature θ and salinity S are formulated as

$$\begin{aligned} \partial_t \theta - \partial_z (\nu'_t \partial_z \theta) &= 0, \\ \partial_t S - \partial_z (\nu'_t \partial_z S) &= 0, \end{aligned} \quad (9)$$

with the eddy diffusivity ν'_t . The hydrographic equations (9) are linked to the hydrodynamic equations (7) by means of an equation of state for potential density,

$$\rho = \rho(\theta, S, p_0), \quad (10)$$

calculated according to Jackett et al. (2006), with the atmospheric pressure at the sea surface, p_0 . Consequently, $\rho_0 = \rho(\theta_0, S_0, p_0)$. Water column stability at a depth with pressure $p_z = \text{const}$, i.e. $\partial_z p_z = 0$, is then calculated as

$$N^2 = \partial_z b = -\frac{g}{\rho_0} \dot{\rho}(\theta, S, p_z) = \partial_\theta \rho(\theta, S, p_z) \partial_z \theta + \partial_S \rho(\theta, S, p_z) \partial_z S, \quad (11)$$

with the Brunt-Väisälä frequency N .

Eddy viscosity ν_t and eddy diffusivity ν'_t are calculated in two ways here. For the analytical calculations presented in Sec. 2.5, 2.5.3, 3 and Appendix A parabolic profiles for ν_t and ν'_t are chosen that extend over the entire thickness of the plume, see Sec. A1 and A2. Such parabolic profiles are often used for well-mixed open channel flow, see the recent discussion by Absi (2021) and allow for analytical treatment of velocity and tracer profiles (Burchard et al., 2013; Lange & Burchard, 2019).

For more realistic simulations that do also allow for predictions of entrainment rates at the base of the plumes, eddy viscosity and eddy diffusivity are determined by means of a two-equation turbulence closure model with an algebraic second-moment closure (Umlauf & Burchard, 2005). This closure is based on an equilibrium assumption for the second moments (turbulent transports of momentum and tracers), that is, the transport terms for the second moments are neglected and only the source and sink terms are retained. The two equations of the closure model represent budgets of the turbulent kinetic energy k and its dissipation rate ε . The eddy coefficients are then calculated as

$$\nu_t = c_\mu (\alpha_N) \frac{k^2}{\varepsilon}, \quad \nu'_t = c'_\mu (\alpha_N) \frac{k^2}{\varepsilon}, \quad (12)$$

where c_μ and c'_μ are quasi-equilibrium (assuming an equilibrium condition for the budget of k only for the second-moment closure) non-dimensional stability functions representing the second-moment closure. The argument of the stability functions is the non-dimensional buoyancy number

$$\alpha_N = \frac{N^2 k^2}{\varepsilon^2}. \quad (13)$$

The weak-equilibrium stability functions that additionally depend on a non-dimensional shear number (Umlauf & Burchard, 2005) are not used since they were found to induce some small-scale oscillations in the entrainment layer at the base of the subglacial plume.

The buoyancy term in the ε equation is calibrated in a way that for homogeneous shear layers in equilibrium the gradient Richardson number converges towards the steady-state value of one quarter (Burchard & Baumert, 1995). This guarantees the correct representation of entrainment rates at the base of surface mixed layers (Umlauf & Burchard, 2005) or on top of dense bottom currents (Umlauf et al., 2010).

In contrast to the second-moment closure used here, C. Cheng et al. (2020) applied the approach of a standard- k - ε model with constant stability functions for their simulations of super-cooled subglacial plumes. In their model, the buoyancy term is not specifically calibrated for reproduction of realistic entrainment rates.

2.2 Boundary conditions

At the upper boundary at $z = z_b$ (ice-ocean interface) a no-slip boundary condition for velocity is fulfilled:

$$u = 0, \quad v = 0, \quad \text{for } z = z_b. \quad (14)$$

The velocity no-slip boundary conditions in (14) are equivalent to the flux boundary conditions

$$-\nu_t \partial_z u = \frac{\tau^{b,x}}{\rho_0} = u_*^{b,x} u_*^b, \quad -\nu_t \partial_z v = \frac{\tau^{b,y}}{\rho_0} = u_*^{b,y} u_*^b, \quad \text{for } z = z_b, \quad (15)$$

with the interfacial shear stress vector $(\tau^{b,x}, \tau^{b,y})$, its absolute value $\tau^b = (u_*^b)^2 \rho_0$ and the interfacial friction velocity $u_*^b = \sqrt{(u_*^{b,x})^2 + (u_*^{b,y})^2}$.

In the framework of this water-column model, the upper boundary is treated as a rigid lid, i.e. melt and freezing processes do not lead to a change in water depth, other than in free-surface models. The dilution of the surface water due to addition of melt water is parameterized here as a virtual salinity flux, see Jenkins et al. (2001) for a discussion of boundary conditions for material (rigid-lid) and immaterial (free-surface) boundary treatment at the ice-ocean interface. Free-surface boundary conditions for freshwater and heat, where the melt water is added to the water column, are given in Sec. 2.3. The diffusive ocean-to-ice fluxes (orthogonal to the ice-ocean interface) of potential temperature and salinity, f_b^T and f_b^S , are located at the same position as the no-slip condition for momentum:

$$-\nu_t' \partial_z \theta = f_b^T, \quad -\nu_t' \partial_z S = f_b^S, \quad \text{for } z = z_b. \quad (16)$$

Note that $Q_M^T = c \rho_0 f_b^T$ is the ocean-to-ice heat flux at the ice-ocean interface, with the heat capacity of ocean water, c . For simplicity, we apply the ocean-to-ice fluxes in the vertical direction, without prior projection from the orthogonal direction. This approximation is valid for small slopes. For example, for a slope of $\tan \alpha_x = 5 \cdot 10^{-3}$ (i.e., a slope angle of 0.28°), the error is about $5 \cdot 10^{-3}$.

Near the boundary, the spatial variation of all momentum and tracer fluxes can be neglected, such that their exact vertical location within the melt layer is not relevant. This plays a role when constructing logarithmic near-boundary profiles based on these fluxes and Dirichlet boundary conditions that are located at slightly different vertical locations (see Sec. 2.4).

The boundary conditions for the turbulent quantities at the ice-ocean interface are best explained by means of near-boundary profiles as functions of the distance from the

interface, $z' = z_b - z$:

$$k(z') = \frac{(u_*^b)^2}{(c_\mu^0)^{1/2}}, \quad \varepsilon(z') = \frac{(u_*^b)^3}{\kappa(z' + z_0)}, \quad (17)$$

where c_μ^0 is the equilibrium stability function for unstratified conditions, κ is the van Karman constant, and z_0 is the hydrodynamic roughness of the ice-ocean interface (see Sec. 2.4 for details). From the turbulence boundary profiles (17) two sets of boundary conditions for $z' = 0$ have been derived, Dirichlet conditions and Neumann conditions, of which Burchard and Petersen (1999) could show that the latter are much more accurate. Note that with (12), the near-interface profile of the eddy viscosity is linear:

$$\nu_t = \kappa u_*^b (z' + z_0). \quad (18)$$

Far away in the ambient and stagnant water with $z \rightarrow -\infty$, the boundary conditions are

$$u = 0, \quad v = 0, \quad \theta = \theta_0, \quad S = S_0, \quad \partial_z k = 0, \quad \partial_z \varepsilon = 0. \quad (19)$$

2.3 Melt rate

To derive formulations for the melt rate and the heat fluxes at the ice-ocean interface, a very thin melt layer at freezing temperature is assumed. The fluxes of potential temperature and salinity across the ice-ocean interface strongly depend on the respective molecular diffusivities, $\nu^T = \nu/\text{Pr}^T$ and $\nu^S = \nu/\text{Pr}^S$, where ν is the molecular viscosity, $\text{Pr}^T = 13.8$ is the Prandtl number for temperature and $\text{Pr}^S = 2432$ is the Schmidt number for salinity.

For the derivation of the melt rate, v_b , i.e., the rate at which water is added to the ocean by means of subglacial melting, we largely follow the paper by D. M. Holland and Jenkins (1999) who compare various formulations. We adopt the well-known three-equation model that is based on flux equilibria of heat and salt across the melt layer and a linear equation for the freezing temperature. With this, the upward heat flux Q_M^T at the ice-ocean interface is composed of the diffusive heat flux Q_I^T into the ice and the latent heat flux Q_L^T needed to melt the ice:

$$Q_M^T = Q_I^T - Q_L^T, \quad (20)$$

with

$$Q_L^T = -\rho_i v_i L_i, \quad (21)$$

where L_i is the latent heat of fusion. Note that $\rho_i v_i$ is the mass of ice per unit time and unit area that is melted, such that v_i is the velocity at which the ice-ocean interface is retreating. The mass of the ocean water that is gained due to melting must be equal to the mass of ice that is melted such that $\rho_i v_i = \rho_0 v_b$, where v_b is the melt rate, i.e., the increase of sea surface height due to melting per unit time. For the flux into the ice, various formulations are available. We adopt the approach based on an advection-diffusion equation of temperature in the glacial ice, with the vertical advection velocity v_i . Based on that, the heat flux into the ice due to diffusion can be formulated as (D. M. Holland & Jenkins, 1999)

$$Q_I^T = -c_i \rho_i v_i (T_I - \theta_b), \quad (22)$$

with the heat capacity of ice, c_i , and the ice-core temperature, T_I . Note that we use here the potential freezing point temperature θ_b instead of the in-situ freezing point temperature T_b , to allow for an easy comparison with the ocean potential temperature. Combining (20) - (22), we obtain for the upward flux of temperature at the ice-ocean interface

$$f_b^T = \frac{Q_M^T}{c \rho_0} = v_b \left(\frac{c_i}{c} (\theta_b - T_I) + \frac{L_i}{c} \right), \quad (23)$$

with the heat capacity of sea water, c . Using the potential melt layer temperature here instead of the in-situ temperature and comparing it to the ice-core temperature here does not pose a problem, due to the large difference between melt layer and ice core temperatures and the typically large uncertainty in the latter.

Since the total salt flux into the glacial ice must be zero, the diffusive salt flux into the melt layer must be assumed to be opposite to the advective salt flux:

$$f_b^S = \frac{Q_M^S}{\rho_0} = v_b S_b. \quad (24)$$

We use a linear equation for the freezing temperature, assuming that the melt layer temperature is at the freezing point:

$$\theta_b = \lambda_1 S_b + \lambda_2 + \lambda_3 z_b \quad (25)$$

with the empirical parameters λ_1 , λ_2 and λ_3 . Note that we use slightly different empirical values than D. M. Holland and Jenkins (1999), to apply the potential temperature of the freezing point instead of its in-situ temperature. The new values have been calculated numerically by means of the function `gsw.t_freezing` of the Gibbs SeaWater (GSW) Oceanographic Toolbox of TEOS-10 at www.teos-10.org, see Tab. 1 for the modified values.

Information about the plume properties in terms of velocity, temperature and salinity are required to close the melt rate computations. This will be provided by either an analytical solution for the vertical structure of the plume (Sec. 2.5) or from a numerical model which uses the analytical model to consistently provide the plume information (Sec. 3.3).

Following Jenkins et al. (2001), the free-surface tracer boundary fluxes can be formulated as

$$\begin{aligned} f_{b,\text{free}}^S &= f_b^S - v_b S_b = 0, \\ f_{b,\text{free}}^T &= f_b^T - v_b \theta_b = v_b \left(\frac{c_i}{c} (\theta_b - T_I) + \frac{L_i}{c} - \theta_b \right). \end{aligned} \quad (26)$$

2.4 Roughness lengths for potential temperature and salinity

Similarly to the classical logarithmic law of the wall for velocity profiles, logarithmic profiles are constructed for temperature and salinity in order to derive numerically consistent boundary conditions. These profiles are highly simplified and do not resolve but parameterize the effects of wall roughness and the viscous sublayer by means of surface roughness lengths. While the boundary condition for the velocity profiles in the melt layer (see Sec. 2.3) is a no-slip condition ($u = v = 0$), boundary values for temperature and salinity in the melt layer are given by $\theta = \theta_b$ and $S = S_b$. It should however be noted that the locations for the boundary values for velocity, temperature and salinity are slightly different. This is due to the substantially different values for kinematic viscosity and the laminar diffusivities for θ and S . These boundary values are formally located at positions slightly above the interface $z = z_b$:

$$\begin{aligned} \theta(z = z_b - [z_0^T - z_0]) &= \theta(z' = z_0^T - z_0) = \theta_b; \\ S(z = z_b - [z_0^S - z_0]) &= S(z' = z_0^S - z_0) = S_b, \end{aligned} \quad (27)$$

where $z_0^T \ll z_0$ and $z_0^S \ll z_0$ are formally defined as tiny roughness lengths specific for temperature and salinity fluxes. The formulations for these roughness parameters given below have been taken from Kader and Yaglom (1972), Yaglom and Kader (1974) and Kader (1981).

For a hydrodynamically rough interface, the roughness length for momentum is given as

$$z_0^{\text{rough}} = k_s \exp(-\kappa B'), \quad (28)$$

where k_s is the characteristic height of the roughness elements and $B' = 8.5$ is an empirical parameter, such that $z_0 \approx k_s/30$. For a hydrodynamically smooth interface

$$z_0^{\text{smooth}} = \nu/u_*^b \cdot \exp(-\kappa B), \quad (29)$$

where $B = 5.5$ is an empirical parameter, such that $z_0 \approx 0.11 \nu/u_*^b$.

For both, hydrodynamically rough and smooth interfaces, the roughness scale with respect to the flux of c (where c represents any tracer such as T or S) is

$$z_0^c = z_0 \exp\left(-\frac{\kappa}{\text{Pr}_t} \beta^c\right), \quad (30)$$

where the value of β^c is calculated differently for rough and smooth interfaces and $\text{Pr}_t = \nu_t/\nu'_t$ is the turbulent Prandtl number. For a hydrodynamically rough interface,

$$\beta_{\text{rough}}^c = 0.55 \exp\left(\frac{1}{2} \kappa B'\right) (z_0^+)^{1/2} \left((\text{Pr}^c)^{2/3} - 0.2\right) - \text{Pr}_t B' + 9.5, \quad (31)$$

with the non-dimensional roughness scale $z_0^+ = z_0 u_*^b / \nu$.

For a hydrodynamically smooth interface, (30) holds with

$$\beta_{\text{smooth}}^c = \left(3.85 (\text{Pr}^c)^{1/3} - 1.3\right)^2 + \text{Pr}_t \left(\frac{\ln \text{Pr}^c}{\kappa} - B\right). \quad (32)$$

The dependence of the tracer roughness length on the Prandtl number is shown in Fig. 1. Note that it is only the logarithms of the roughness lengths that are evaluated and not their direct values (which are partially too tiny to be computed). Furthermore, (30) and (32) are valid for $z_0^+ < 0.1$ and (29) and (31) are valid for $z_0^+ > 3.33$. Here we concentrate on the rough wall conditions and therefore set $z_0 = z_0^{\text{rough}}$ and $\beta^c = \beta_{\text{rough}}^c$.

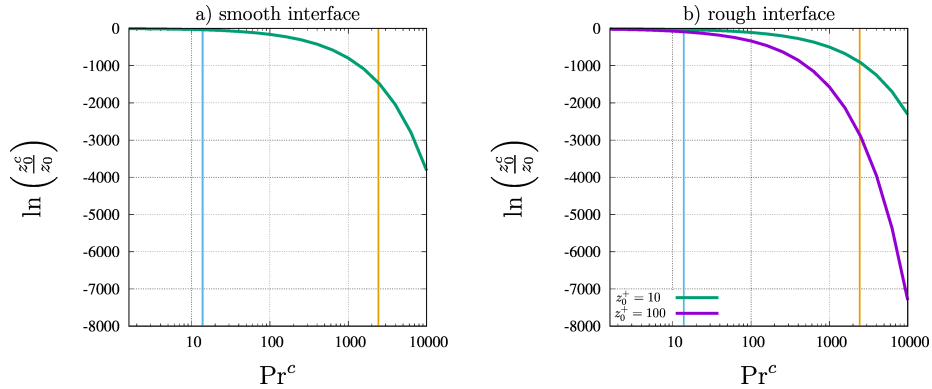


Figure 1. Logarithm of relative roughness length for tracers for a) smooth and b) rough interfaces as function of the molecular Prandtl number. The Prandtl number Pr^T for temperature (blue) and the Schmidt number Pr^S for salinity (yellow) are indicated as vertical lines. The two curves in panel b represent two different roughness lengths z_0^+ .

2.5 Analytical plume model

The analytical plume model that is derived here serves two purposes: It is used to construct consistent discrete formulations for the boundary conditions for θ and S (see Sec. 3) and it is used to perform an analytical parameter space study for subglacial plumes. To allow for an analytical solution, Earth rotation is neglected ($f = 0$ in equation (7)), such that only one velocity component needs to be taken into consideration. Furthermore, the interfacial slope is assumed to be positive, such that $u_*^{b,x} = u_*^b > 0$. At the plume base, turbulent entrainment of ambient water is assumed by prescribed values of friction velocity u_*^s , turbulent temperature flux f_a^T and turbulent salinity flux f_a^S . A further simplification is that for the pressure gradient force, the buoyancy of the plume is assumed to be constant: $b = \text{const}$. The profiles are formulated as a function of prescribed depth-mean values of velocity, potential temperature and salinity, \bar{u} , $\bar{\theta}$ and \bar{S} . The profiles are calculated over the entire plume thickness D , assuming parabolic eddy viscosity and eddy diffusivity. For simplicity the distance from the ice-ocean interface $z' = z_b - z$ is used as vertical reference.

2.5.1 Velocity profile

The derivation of the analytical stationary velocity profile under a sloping ice-ocean interface is shown in Sec. A1:

$$u(z') = \frac{\bar{u}}{A} \ln \left[\frac{z' + z_0}{z_0} \right] - \frac{u_*^s |u_*^s|}{\kappa u_*^b} \frac{D}{D + z_0} \left(\frac{1}{A} \ln \left[\frac{z' + z_0}{z_0} \right] + \ln \left[\frac{D - z'}{D} \right] \right), \quad (33)$$

where u_*^b will be calculated by means of solving the quadratic equation (A9), and A is a non-dimensional integration constant defined in (A10). The first term in (33) is the classical logarithmic law of the wall written in a form where its vertical average is \bar{u} . The second term represents the effect of the entrainment of ambient water at the plume base. It has a vertical average of zero and diverges to $\pm\infty$ for $z' \rightarrow D$, depending on the sign of u_*^s . A similar solution had been proposed by Lange and Burchard (2019) for the effect of surface wind stress in estuarine exchange flow.

2.5.2 Tracer profiles

With (A20), neglecting a tiny exponential expression in the term representing the effect of entrainment, we can formulate the analytical profiles for potential temperature ($c = \theta$) and salinity ($c = S$) as follows:

$$\begin{aligned} \theta(z') = & \theta_b + \frac{\text{Pr}_t f_b^T}{\kappa |u_*^b|} \left(\ln \left[\frac{z' + z_0}{z_0} \right] + \frac{\kappa}{\text{Pr}_t} \beta^T \right) \\ & - \frac{\text{Pr}_t f_s^T}{\kappa |u_*^b|} \left(\frac{z_0}{D + z_0} \left(\ln \left[\frac{z' + z_0}{z_0} \right] + \frac{\kappa}{\text{Pr}_t} \beta^T \right) + \frac{D}{D + z_0} \ln \left[\frac{D - z'}{D + z_0} \right] \right), \end{aligned} \quad (34)$$

and

$$\begin{aligned} S(z') = & S_b + \frac{\text{Pr}_t f_b^S}{\kappa |u_*^b|} \left(\ln \left[\frac{z' + z_0}{z_0} \right] + \frac{\kappa}{\text{Pr}_t} \beta^S \right) \\ & - \frac{\text{Pr}_t f_s^S}{\kappa |u_*^b|} \left(\frac{z_0}{D + z_0} \left(\ln \left[\frac{z' + z_0}{z_0} \right] + \frac{\kappa}{\text{Pr}_t} \beta^S \right) + \frac{D}{D + z_0} \ln \left[\frac{D - z'}{D + z_0} \right] \right), \end{aligned} \quad (35)$$

with the potential temperature θ_b and the salinity S_b of the melt layer. As for the velocity profile (33), also the profiles of potential temperature and salinity diverge towards $\pm\infty$ for $z' \rightarrow D$, but also here the vertical averages are finite.

It should be noted that the boundary values for potential temperature and salinity do not converge to θ_b and S_b for $z' \rightarrow 0$. This is also the case for the classical logarithmic laws with zero entrainment fluxes f_s^T and f_s^S . This inconsistency results from

the strong gradients of θ and S in the melt layer due to their small Schmidt numbers. However, since the fluxes of θ and S across the melt layer are applied as boundary conditions and since they are assumed to be constant within the boundary layer, this inconsistency is acceptable. This is clearly seen in the analytical profiles shown in Fig. 2b,c and the values given in the caption.

Vertical averaging of (34) and (35) gives

$$\bar{\theta} - \theta_b = \frac{\text{Pr}_t f_b^T}{\kappa |u_*^b|} A_T - \frac{\text{Pr}_t f_s^T}{\kappa |u_*^b|} \left(\frac{z_0}{D + z_0} A_T - \frac{D}{D + z_0} \left(1 - \ln \left[\frac{D}{D + z_0} \right] \right) \right), \quad (36)$$

and

$$\bar{S} - S_b = \frac{\text{Pr}_t f_b^S}{\kappa |u_*^b|} A_S - \frac{\text{Pr}_t f_s^S}{\kappa |u_*^b|} \left(\frac{z_0}{D + z_0} A_S - \frac{D}{D + z_0} \left(1 - \ln \left[\frac{D}{D + z_0} \right] \right) \right), \quad (37)$$

with the integration constants A_T and A_S calculated according to (A22). By combining (34) and (35) with (36) and (37), a formulation of the profiles is obtained that depends on prescribed values of the depth-averaged potential temperature $\bar{\theta}$ and salinity \bar{S} . The melt layer freezing temperature and melt layer salinity θ_b and S_b can now be determined, using the melt layer formulation given in Sec. 2.3. Combining equations (23) and (24) for the interface fluxes of potential temperature and salinity, the linear freezing temperature formulation (25) with the vertically averaged equations (36) and (37) for potential temperature and salinity of the plume gives five equations for the five unknowns f_b^T , f_b^S , v_b , T_b and S_b . These equations are combined in a way that a quadratic equation for S_b results, of which the positive solution is the physically correct one.

2.5.3 Analytical examples

Two sets of plume profiles are calculated, without entrainment at the plume base (experiment N) and with entrainment at the plume base (experiment E). Results for u , θ and S are shown in Fig. 2, using the empirical parameters given in table 1. For both experiments, bulk values of the plume thickness $D = 20$ m, the depth-mean velocity $\bar{u} = 0.2 \text{ m s}^{-1}$, the depth-mean temperature $\bar{\theta} = -1.75^\circ\text{C}$, the depth-mean salinity $\bar{S} = 33.1 \text{ g kg}^{-1}$, the interfacial depth $z_b = -300$ m, and an interfacial roughness length of $z_0 = 10^{-2}$ m are prescribed. These values are similar to those at the end of the transient default experiment from Sec. 4.2.1. Results are shown in linear and logarithmic scale.

For the experiment without entrainment, the profiles of velocity, temperature and salinity are exactly logarithmic (Fig. 2d-f). Due to the small Schmidt numbers, the slopes of the temperature and salinity profiles are very small. In the case of salinity, the difference across the full depth of the plume is about only $6 \cdot 10^{-3} \text{ g kg}^{-1}$, such that in the non-logarithmic presentation (Fig. 2c), vertical salinity gradients can not be detected by visual inspection. A striking feature of the analytical temperature and salinity profiles is the substantial difference between the melt layer values, θ_b and S_b , and the boundary values, $\theta(z_b)$ and $S(z_b)$, see Fig. 2b,c. This is a direct consequence of (27), and does not pose a practical problem, because it is not the boundary values that are applied, but the fluxes of temperature and salinity which are assumed to be constant on the scale of the melt layer thickness. There is a conceptual issue, because the construction of the free-surface boundary conditions assumes that melt layer values and boundary values are identical (see Jenkins et al., 2001, and Eq. (26) of this study). Since these free-surface boundary conditions are not used here, it is beyond the scope of the present study to resolve this inconsistency.

The analytical solution including fluxes of momentum, temperature and salinity across the base of the plume (exp. E, Fig. 2g-l) allows to mimic entrainment of ambient water. The entrainment fluxes are estimated as follows:

$$u_*^s |u_*^s| = -v_e (\bar{u} - u_0), \quad f_s^T = -v_e (\bar{\theta} - \theta_0), \quad f_s^S = -v_e (\bar{S} - S_0), \quad (38)$$

with the entrainment velocity $v_e = 0.036 \bar{u} \sin \alpha$, see Jenkins (1991) and Sec. 4.3, and the ambient values are chosen to be the same as in the default scenario of the transient simulations presented in Sec. 4.2.1: $\tan \alpha = 0.005$, $u_0 = 0$, $\theta_0 = 1^\circ\text{C}$ and $S_0 = 34.5 \text{ g kg}^{-1}$. With the above parameters, we obtain $v_e = 3.6 \cdot 10^{-5} \text{ m s}^{-1}$, $u_*^s = -7.6 \cdot 10^{-6} \text{ m s}^{-1}$, $f_s^T = 9.9 \cdot 10^{-5} \text{ K m s}^{-1}$ and $f_s^S = 5.0 \cdot 10^{-5} \text{ g kg}^{-1} \text{ m s}^{-1}$.

As a result, the entrainment has only a minimal influence on the velocity and salinity profiles (Figs. 2g,j and 2i,l). However, the temperature profile (Figs. 2h,k) shows slightly larger vertical gradients due to the entrainment of relatively warm water. Due to the stationary character of the analytical solution with fixed values of \bar{u} , $\bar{\theta}$ and \bar{S} , there is no predictive skill. The melt rate ($v_m = 5.22 \text{ m y}^{-1}$) and the ocean-to-ice heat flux ($Q_M^T = 63 \text{ W m}^{-2}$) depend only weakly on the entrainment. But due to entrainment of warm and salty ambient water, the instantaneous trends in average plume temperature and salinity are changed from $\partial_t \bar{T} = -6.3 \cdot 10^{-2} \text{ K day}^{-1}$ to $\partial_t \bar{T} = +0.37 \text{ K day}^{-1}$ and from $\partial_t \bar{S} = -2.2 \cdot 10^{-2} \text{ g kg}^{-1} \text{ day}^{-1}$ to $\partial_t \bar{S} = +0.19 \text{ g kg}^{-1} \text{ day}^{-1}$.

Variable	Meaning	Value	Unit
c	heat capacity of sea water	4180.0	$\text{J kg}^{-1} \text{K}^{-1}$
c_i	heat capacity of glacial ice	1995.0	$\text{J kg}^{-1} \text{K}^{-1}$
κ	van Karman number	0.4	–
λ_1	parameter in freezing temperature equation	-0.0567	$\text{K (g kg}^{-1})^{-1}$
λ_2	parameter in freezing temperature equation	0.0754	K
λ_3	parameter in freezing temperature equation	$7.68 \cdot 10^{-4}$	K m^{-1}
L_i	latent heat of fusion	$3.335 \cdot 10^5$	J kg^{-1}
Pr_t	turbulent Prandtl number	0.7	–
Pr^T	molecular Prandtl number for T	13.8	–
Pr^S	molecular Prandtl number for S	2432.0	–
ν	molecular viscosity	$1.95 \cdot 10^{-6}$	$\text{m}^2 \text{s}^{-1}$
ρ_0	reference density of ocean water	1027	kg m^{-3}
ρ_i	density of glacial ice	910	kg m^{-3}
T_I	ice core temperature	-20.0	$^\circ\text{C}$

Table 1. Table summarising the empirical parameters used in the present study.

3 Numerical implementation

In numerical models, the analytical logarithmic profiles for u , θ and S derived in Sec. 2.5 can be used to calculate fluxes of momentum, temperature and salinity at the ice-ocean interface in a consistent and convergent way. To do so, we assume that within the first grid layer underneath the ice-ocean interface the logarithmic laws (33), (34) and (35) are valid, neglecting the fluxes across the plume base ($u_*^s = f_s^T = f_s^S = 0$), such that the formulations reduce to

$$u(z') = \frac{u_*^{b,x}}{\kappa} \ln \left[\frac{z' + z_0}{z_0} \right], \quad v(z') = \frac{u_*^{b,y}}{\kappa} \ln \left[\frac{z' + z_0}{z_0} \right], \quad (39)$$

$$\theta(z') = \theta_b + \frac{\text{Pr}_t f_b^T}{\kappa u_*^b} \left(\ln \left[\frac{z' + z_0}{z_0} \right] + \frac{\kappa}{\text{Pr}_t} \beta^T \right), \quad (40)$$

and

$$S(z') = S_b + \frac{\text{Pr}_t f_b^S}{\kappa u_*^b} \left(\ln \left[\frac{z' + z_0}{z_0} \right] + \frac{\kappa}{\text{Pr}_t} \beta^S \right), \quad (41)$$

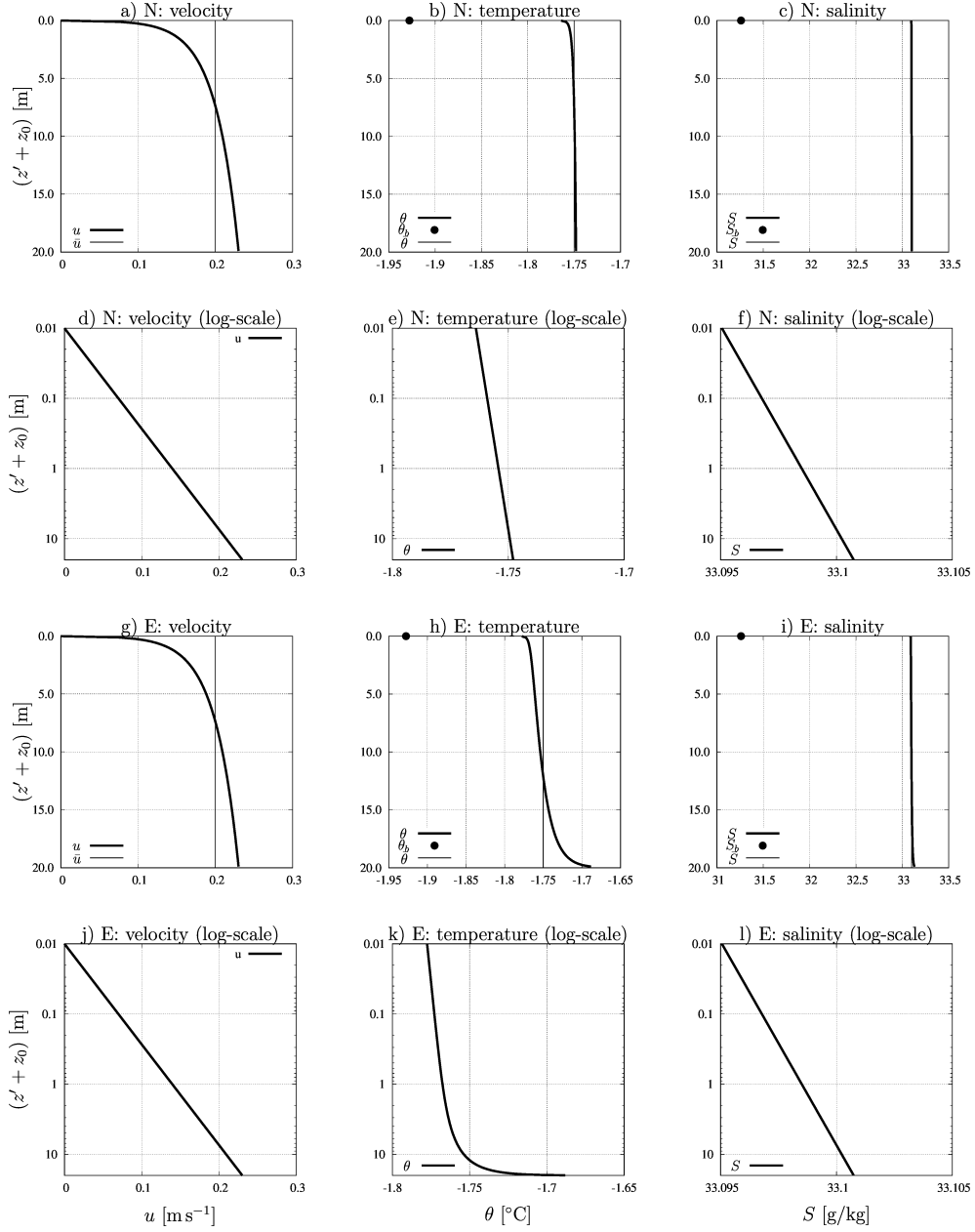


Figure 2. Analytical solutions for velocity (panels a, d, g j), potential temperature (panels b, e, h, k) and salinity (panels c, f, i, l) for experiments N (without entrainment, panels a-f) and E (with entrainment panels g-l). Parameter values are given in Tab. 1. Profiles are shown as bold lines in linear (panels a-c,g-i) and logarithmic (panels d-f, j-l) depth scale. Prescribed depth mean values \bar{u} , $\bar{\theta}$ and \bar{S} are shown as thin lines. Boundary values $T(z_b - (z_0 - z_0^T)) = T_b$, and $S(z_b - (z_0 - z_0^S)) = S_b$, are shown as symbols. Note that $S_b = 31.26 \text{ g kg}^{-1}$ is substantially smaller than $S(z_b) = 33.09 \text{ g kg}^{-1}$, and $\theta_b = -1.93 \text{ }^\circ\text{C}$ is substantially smaller than $\theta(z_b) = -1.76 \text{ }^\circ\text{C}$.

where we have extended the analytical solution to the full velocity vector (u, v) . Note, that the analytical profiles (39) - (41) are expected to hold in some vicinity of the interface only, depending on the forcing of the plume.

3.1 Momentum fluxes

Let in a numerical model $u(z'_{k_{\max}}) = u_{k_{\max}}$ and $v(z'_{k_{\max}}) = v_{k_{\max}}$ denote the upper-layer velocity vector with the upper layer thickness $h_{k_{\max}}$ and $z'_{k_{\max}} = \frac{1}{2}h_{k_{\max}}$. Then (39) gives

$$u_{k_{\max}} = \frac{u_*^{b,x}}{\kappa} \ln \left(\frac{\frac{1}{2}h_{k_{\max}} + z_0}{z_0} \right), \quad v_{k_{\max}} = \frac{u_*^{b,y}}{\kappa} \ln \left(\frac{\frac{1}{2}h_{k_{\max}} + z_0}{z_0} \right), \quad (42)$$

such that

$$u_*^{b,x} u_*^b = c_d u_{k_{\max}} (u_{k_{\max}}^2 + v_{k_{\max}}^2)^{1/2}, \quad u_*^{b,y} u_*^b = c_d v_{k_{\max}} (u_{k_{\max}}^2 + v_{k_{\max}}^2)^{1/2}, \quad (43)$$

with the numerical drag coefficient

$$c_d = \left(\frac{\kappa}{\ln \left(\frac{\frac{1}{2}h_{k_{\max}} + z_0}{z_0} \right)} \right)^2. \quad (44)$$

This is the numerically consistent discretization for the momentum flux at the ice-ocean interface as defined in (15). At the same time, (43) with (44) also satisfy the no-slip condition (14) for u and v , since with fixed left-hand sides in (43) a decreasing surface layer thickness $h_{k_{\max}}$ will lead to unbounded growth of c_d and thus convergence of $u_{k_{\max}}$ and $v_{k_{\max}}$ towards zero. This numerical treatment of a frictional boundary layer is applied in many ocean models for the bottom boundary layer (Klingbeil et al., 2018, their Sec. 7.6). If, however, a constant value for c_d is chosen that does not depend on resolution, then a refined resolution near the boundary will not result in a reduction of velocity and consequently in an underestimation of shear and friction velocity (see Sec. 3.4).

3.2 Tracer fluxes

The calculations of the temperature and salinity fluxes are carried out in a similar way than the momentum fluxes. When for the discrete profiles of temperature and salinity, $\theta(z'_{k_{\max}}) = \theta_{k_{\max}}$ and $S(z'_{k_{\max}}) = S_{k_{\max}}$ with $z'_{k_{\max}} = \frac{1}{2}h_{k_{\max}}$ and the upper layer thickness $h_{k_{\max}}$ are known, the following relations can be derived from the logarithmic tracer laws (40) and (41):

$$\theta_{k_{\max}} = \theta_b + \frac{\text{Pr}_t f_b^T}{\kappa u_*^b} \left(\ln \left[\frac{\frac{1}{2}h_{k_{\max}} + z_0}{z_0} \right] + \frac{\kappa}{\text{Pr}_t} \beta^T \right), \quad (45)$$

and

$$S_{k_{\max}} = S_b + \frac{\text{Pr}_t f_b^S}{\kappa u_*^b} \left(\ln \left[\frac{\frac{1}{2}h_{k_{\max}} + z_0}{z_0} \right] + \frac{\kappa}{\text{Pr}_t} \beta^S \right). \quad (46)$$

Note that (45) and (46) can be reformulated as

$$f_b^T = \gamma^T (\theta_{k_{\max}} - \theta_b) \quad (47)$$

and

$$f_b^S = \gamma^S (S_{k_{\max}} - S_b) \quad (48)$$

with the exchange velocities

$$\gamma^T = \frac{\kappa u_*^b}{\text{Pr}_t \ln \left(\frac{\frac{1}{2}h_{k_{\max}} + z_0}{z_0} \right) + \kappa \beta^T} \quad (49)$$

and

$$\gamma^S = \frac{\kappa u_*^b}{\text{Pr}_t \ln \left(\frac{\frac{1}{2} h_{k_{\max}} + z_0}{z_0} \right) + \kappa \beta^S} \quad (50)$$

with the coefficients β^T and β^S from (31) or (32). With (23), (24), (25), (47) and (48) we have now five equations to solve for the five unknowns T_b , S_b , v_b , f_b^T and f_b^S . Note that we solve this system of equations in order to calculate the melt rate v_b which is applied to add fresh and cold water to the ocean surface due to subglacial melting, see Sec. 3.3 for the implementation.

3.3 Free-surface versus rigid-lid models

For a free-surface model, $h_{k_{\max}}^n$ and the tracer concentration $X_{k_{\max}}^n$ should be discretized as follows (assuming zero volume and tracer fluxes across the interface at the bottom of the layer):

$$\frac{h_{k_{\max}}^{n+1} - h_{k_{\max}}^n}{\Delta t} = v_b^n, \quad (51)$$

and

$$\frac{X_{k_{\max}}^{n+1} h_{k_{\max}}^{n+1} - X_{k_{\max}}^n h_{k_{\max}}^n}{\Delta t} = - (f_{b,\text{free}}^X)^n, \quad (52)$$

which can be combined into

$$h_{k_{\max}}^{n+1} \frac{X_{k_{\max}}^{n+1} - X_{k_{\max}}^n}{\Delta t} = -v_b^n X_{k_{\max}}^n - (f_{b,\text{free}}^X)^n, \quad (53)$$

where the superscript indicates the number of the time step. For a rigid-lid model as applied in the present study, the numerical scheme (53) will apply, but with a constant layer thickness $h_{k_{\max}}$:

$$\frac{X_{k_{\max}}^{n+1} - X_{k_{\max}}^n}{\Delta t} = - \frac{v_b^n X_{k_{\max}}^n + (f_{b,\text{free}}^X)^n}{h_{k_{\max}}}, \quad (54)$$

where the respective free-surface fluxes for temperature and salinity are calculated according to (26).

3.4 Numerical convergence experiment

To test the numerical methods developed in Sec. 3.1 - 3.3, the momentum equation (7) for non-rotational flow ($f = 0$ and $v = 0$) and the temperature and salinity equations (9) were discretized. The entire water column was accelerated by a barotropic (constant in space) pressure gradient in a way that the prescribed depth-averaged plume velocity of \bar{u} resulted. Additionally to the melt fluxes, temperature and salinity were forced with a depth-independent source/sink term compensating for the freshening and cooling, see (A18). Empirical parameters were chosen identically to Experiment N in Sec. 2.5.3, such that an analytical solution is available for quantifying the accuracy of the numerical scheme for different vertical resolutions and treatments of the melt flux parameterization.

An Euler-forward central-difference discretization of these diffusion equations was applied with a sufficiently small time step. The numerical scheme was executed until a stationary numerical solution was approximated at high accuracy. Three different vertical discretizations were chosen, ranging from very coarse to very fine (see details in the caption of Tab. 2).

For each vertical resolution, three different numerical treatments of the melt fluxes were chosen:

1. The high-resolution accurate treatment as given by (42), (45) and (46) with the analytical logarithmic laws for momentum and tracers.

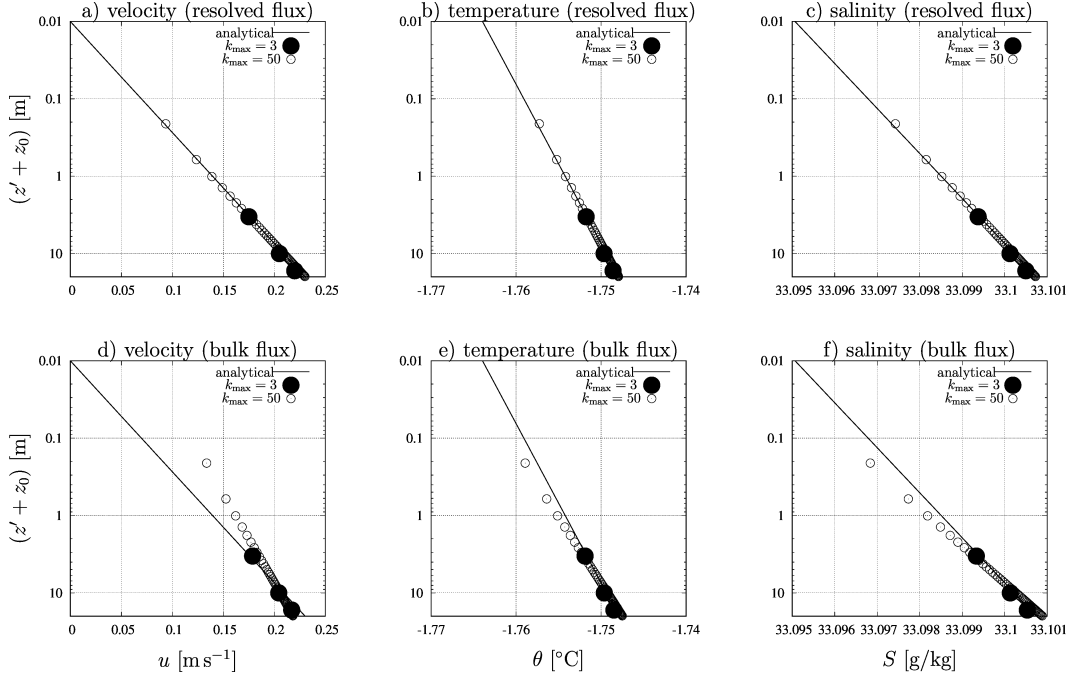


Figure 3. Numerical simulation of experiment N without entrainment at the plume base: Numerical simulations for velocity u (panels a & d) potential temperature θ (panels b & e) and salinity S (panels c & f) in logarithmic scale using values given in table 1. The analytical solution is shown by a black line, the numerical solutions are shown by large black dots ($k_{\max} = 3$) and small circles ($k_{\max} = 50$). Panels a-c show profiles obtained from the high-resolution numerical flux calculations derived in Sec. 3.1 and 3.2 (method 1). In panels d-f numerical profiles are shown where bulk flux parameterizations were used by inserting in the formulations (42) - (50) the plume thickness D instead of the upper layer thickness $h_{k_{\max}}$ and the plume-average values \bar{u} , $\bar{\theta}$ and \bar{S} instead of the upper layer values $u_{k_{\max}}$, $\theta_{k_{\max}}$ and $S_{k_{\max}}$ (method 3).

2. The high-resolution formulation (42) for momentum, but bulk values across the entire plume thickness for the tracer fluxes, i.e., using (45) and (46) with the plume thickness D instead of the upper layer thickness $h_{k_{\max}}$ and the plume-average values $\bar{\theta}$ and \bar{S} instead of the upper layer values $\theta_{k_{\max}}$ and $S_{k_{\max}}$.
3. Similar to 2., but now also for the momentum flux calculation a bulk formulation is used by using (42) with D and \bar{u} instead of $h_{k_{\max}}$ and $u_{k_{\max}}$.

Numerical results for method 1 are shown in Fig. 3a-c against the analytical solution for two different resolutions. The results are highly accurate, even for the coarse resolution with only three layers inside the plume. Results for method 2 are very similar (not shown). This means that the bulk formulation for the tracer fluxes is still valid because of the high vertical homogeneity of the tracer profiles with $\theta_{k_{\max}} \approx \bar{\theta}$ and $S_{k_{\max}} \approx \bar{S}$ and γ^T and γ^S being largely independent of the layer thickness. In contrast, method 3 diverges from the analytical reference solution (see Fig. 3d-f), since the bulk formulation for the momentum flux is decreasingly representative for increasing resolution with c_d not increasing towards ∞ .

Since the accurate calculation of the melt rate v_b is one of the main goals of refined numerical simulations, it is given in Tab. 2 for all numerical experiments (three resolutions and three melt flux formulations). For the consistent melt flux formulation 1, melt

		u resolved θ & S resolved Fig. 3a-c	u resolved θ & S bulk	u bulk θ & S bulk Fig. 3d-f
analytical		5.2236		
$k_{\max} = 3$;	$h_{k_{\max}} = 6.66$ m	5.2070	5.1962	4.7888
$k_{\max} = 50$;	$h_{k_{\max}} = 0.4$ m	5.2710	5.2546	4.0944
$k_{\max} = 200$;	$h_{k_{\max}} = 0.015$ m	5.2360	5.2226	3.6353

Table 2. Numerical simulation of experiment N without entrainment at the plume base: Calculated subglacial melt rates in m y^{-1} for various vertical resolutions and different treatments of fluxes, compared to the analytical melt rate. The very high resolution for $k_{\max} = 200$ layers was obtained by logarithmic zooming towards the ice-ocean interface.

rates converge towards the analytical value of 5.2236 m y^{-1} . In the range of the resolutions tested here, method 2 shows an almost indistinguishable behaviour, although it should formally not converge towards the analytical solution. Also for the coarse resolutions both methods 1 and 2 give relatively accurate values with only about 3-4 % error for the very coarse resolution. In contrast to this, the bulk method 3 for calculating momentum fluxes diverges substantially, and gives an error of about 1.1 m y^{-1} (22 %) for a top-layer resolution of $h_{k_{\max}} = 0.4$ m, and an error of 1.6 m y^{-1} (30 %) for the very high resolution of $h_{k_{\max}} = 0.015$ m. Therefore, it is highly recommended to use methods 1 or 2 for the momentum and tracer fluxes, with a preference for the fully consistent method 1.

4 Transient numerical experiments

The General Ocean Turbulence Model (GOTM, Burchard and Bolding (2001); Umlauf and Burchard (2005); Li et al. (2021), see also www.gotm.net), a one-dimensional water-column model coupled to a library of turbulence closure models, was modified to reproduce the vertical structure of subglacial plumes. For the surface, i.e., the ice-ocean interface, no-slip conditions for velocity (14) and fluxes of salinity and heat due to melt processes at the ice-ocean interface (16) were added. Since GOTM treats surface freshwater fluxes like a rigid-lid model (i.e., considering changes in concentrations instead of changes in volume), the fluxes of salinity and heat have been implemented according to (54). A further change to GOTM needed to reproduce subglacial plumes was the application of pressure gradients due to vertical buoyancy gradients under a sloping ice-ocean interface, as described in (5). As turbulence closure model, the k - ε model with the quasi-equilibrium second-moment closure by Y. Cheng et al. (2002) was used.

4.1 Model setup

The simulations analysed here start from rest (zero velocity). The initial values of potential temperature and salinity within the plume of initially $D = 5$ m thickness represent ambient seawater mixed with fresh water at freezing temperature to mimic subglacial discharge at the grounding line (supposed to be at a depth of $z_b = -300$ m). The depth of the water column is chosen to be 150 m, such that the bottom at $z = -450$ m is sufficiently deep to allow for an undisturbed plume deepening for all sensitivity studies. The vertical discretisation uses $k_{\max} = 500$ layers with zooming towards the ice-ocean interface such that the resolution is gradually increasing from $h_1 = 0.5$ m at the

bottom to $h_{k_{\max}} = 0.09$ m at the surface. In a sensitivity study about the effects of coarser vertical resolution, a total of only 50 or 25 layers will be used (Sec. 4.2.3).

The ambient water is at rest and has a high ocean salinity of $S_0 = 34.5 \text{ g kg}^{-1}$ and potential temperatures of $\theta_0 = 1^\circ\text{C} \pm 1^\circ\text{C}$ (depending on the scenario). The initial plume salinity and potential temperature are $S = 32 \text{ g kg}^{-1}$ and $\theta = -1^\circ\text{C}$, such that its potential density ρ is lower than the potential density ρ_0 of the plume water. With this, the initial pressure gradient drives a subglacial plume rising upwards along the slope of the ice-ocean interface. The latitude of the water column location is 79°N , such that the Coriolis parameter has a value of $f = 1.43 \cdot 10^{-4} \text{ s}^{-1}$. The ice-ocean interface is sloping towards the north, while the slope toward the east vanishes ($\alpha_x = 0$). During the simulation time of 14 days, the plume velocity is expected to point towards the north-east ($u, v > 0$) directions as a consequence of the force balance between northward pressure gradient force, Coriolis force and frictional effects. The plume is subject to cooling and freshening due to melt fluxes at the ice-ocean interface and to warming and salinification due to entrainment of warmer and saltier ambient water. This simulation can be thought of as a plume underneath an infinite plain, where all plume properties are homogeneous along the interfacial slope (Arneborg et al., 2007), and all thermodynamic effects of the interfacial slope are ignored.

We analyse one default simulation in detail and carry out six sensitivity simulations with variations in northward slope α_y , interfacial roughness z_0 and ambient temperature θ_0 . The parameters for the sensitivity study are given in table 3.

	high	default	low
	ayp	def	aym
$\tan \alpha_y$:	$2.5 \cdot 10^{-2}$	$5 \cdot 10^{-3}$	$1 \cdot 10^{-3}$
	z0p	def	z0m
z_0^b :	$1 \cdot 10^{-1} \text{ m}$	$1 \cdot 10^{-2} \text{ m}$	$1 \cdot 10^{-3} \text{ m}$
	tap	def	tam
θ_0 :	2°C	1°C	0°C

Table 3. Parameter settings for the default simulation (**def**) and sensitivity simulations with high (**ayp**) and low (**aym**) values for the interfacial slope α_y , high (**z0p**) and low (**z0m**) values for the interfacial roughness z_0^b and high (**tap**) and low (**tam**) values for the ambient temperature θ_0 .

4.1.1 Analysis of bulk values

According to Arneborg et al. (2007), the bulk properties of the plume can be diagnosed from individual profiles as follows:

$$\begin{aligned}
 \bar{b}D &= \int_{-\infty}^{z_b} b \, dz, \\
 \bar{b}D^2 &= 2 \int_{-\infty}^{z_b} b(z_b - z) \, dz, \\
 (\bar{u}D, \bar{v}D) &= \int_{-\infty}^{z_b} (u, v) \, dz,
 \end{aligned} \tag{55}$$

with the plume thickness D , the depth-averaged buoyancy \bar{b} , and the depth-averaged plume velocity vector (\bar{u}, \bar{v}) . The vertically averaged plume speed is defined as $\bar{u}_s = (\bar{u}^2 + \bar{v}^2)^{1/2}$.

Depth-averaged salinity and potential temperature are defined accordingly:

$$\bar{S} = \frac{1}{D} \int_{-\infty}^{z_b} (S - S_0) dz + S_0 \text{ and } \bar{\theta} = \frac{1}{D} \int_{-\infty}^{z_b} (\theta - \theta_0) dz + \theta_0. \quad (56)$$

Characteristic non-dimensional parameters of the plume dynamics are the Froude number (ratio of flow velocity to phase velocity of long interfacial waves)

$$\text{Fr} = \frac{\bar{u}_s}{\sqrt{\bar{b}D \cos \alpha}}, \quad (57)$$

where $\text{Fr} > 1$ marks supercritical flow and $\text{Fr} < 1$ marks subcritical flow, the Ekman number (ratio of frictional to rotational effects)

$$K = \frac{c_d \bar{u}_s}{fD} \quad (58)$$

and the bulk Richardson number (ratio of bulk stratification to bulk shear)

$$\text{Ri}_b = \frac{\bar{b}D}{\bar{u}_s^2} \approx \text{Fr}^{-2}, \quad (59)$$

which we need to define for the entrainment formulation by Jungclaus and Backhaus (1994). For the Froude number, the overall slope angle is calculated as

$$\alpha = \arctan \left(\tan^2 \alpha_x + \tan^2 \alpha_y \right)^{1/2}. \quad (60)$$

4.2 Model Results

4.2.1 Default scenario

In the default scenario, the plume thickness increases from its initial value of $D = 5$ m to about $D = 20$ m within 14 days (Fig. 4). In the initial phase, the plume is accelerated northwards along the slope due to the pressure gradient force, reaching up to a depth-averaged value of $\bar{v} = 0.25 \text{ m s}^{-1}$ within one hour (Fig. 5a). In this initial phase, the flow is supercritical ($\text{Fr} > 1$) for a short time (Fig. 5b). Afterwards, due to Earth rotation, the plume velocity veers towards the cross-slope direction (Fig. 4a,b). This effect is strongest at the plume base where frictional and rotational effects combine in a complex way (Fig. 6d), see Fig. 11 of Umlauf et al. (2010) for details. During the further development of the plume, frictional effects are reduced due to increased plume thickness and decreased velocity (expressed as strongly decreasing Ekman number, see Fig. 5b), such that the depth-averaged velocity vector (\bar{u}, \bar{v}) is further veering towards the downslope direction (Fig. 5a), with the downslope velocity peak remaining at the plume base. After the initial adjustment phase, the plume is close to a dynamic balance as indicated by the relatively close agreement between plume velocity diagnosed from the simulation result and the analytical equilibrium velocity diagnosed from the dynamic steady-state assumption of the vertically integrated momentum equations (see Appendix B).

After the initialization, the flow becomes subcritical, with the Froude number slowly decreasing to $\text{Fr} = 0.6$ at the end of the simulation (Fig. 5b). The square root of the vertically integrated and thus the shallow-water speed $(\bar{b}D)^{1/2}$ is slowly increasing during simulation due to the buoyancy fluxes at the ice-ocean interface (Fig. 5a). For no such buoyancy fluxes theory predicts a constant shallow water speed (Arneborg et al., 2007). Potential temperature and salinity are quickly approaching relatively constant values, suggesting a balance between melt fluxes and entrainment fluxes (Fig. 4c,d).

Since the vertical structure of the plume is almost self-similar after the initial adjustment (Arneborg et al., 2007), the vertical profiles of plumes properties shown in Fig. 6 at the end of the simulation time are largely representative for the plume in dynamical balance. When rotating the velocity vector profiles into the direction of the depth

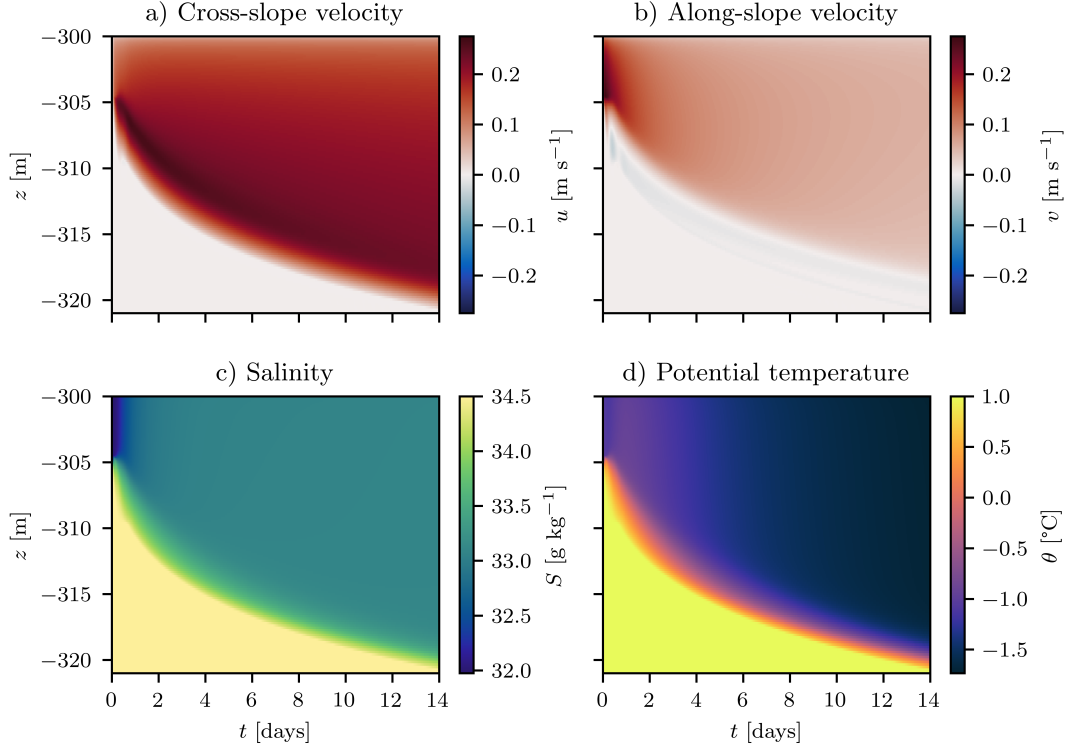


Figure 4. Simulated cross-slope and along-slope velocity, salinity and potential temperature profiles for the default scenario **def** during the 14-day simulation period.

mean flow vector, it becomes evident that the velocity peak at the plume base is most pronounced in the cross-flow velocity component (Fig. 6a). In the frictionally dominated part of the plume, the cross-flow velocity is negative due to Ekman dynamics (Umlauf & Arneborg, 2009; Umlauf et al., 2010). Potential temperature and salinity are well-mixed in the bulk of the plume, with a gradual increase in stratification at the plume base (Fig. 6b,c). The entire plume is stably stratified (Fig. 6d). Most of the stratification seems to be due to entrainment of denser water from below, but the increase of N^2 towards the ice-ocean interface indicates that some stratification is also induced by the stabilising ocean-to-ice fluxes. Due to the strong shear at the ice-ocean interface (Fig. 6e), the gradient Richardson number decreases continuously in upward direction. It has a maximum of about $\text{Ri} = 0.75$ directly above the entrainment layer. It is characteristic of two-equation turbulence closure models that they allow active mixing at such high stability conditions due to vertical turbulent transport of TKE (Umlauf, 2009). In the entrainment layer itself, Ri attains the value of the steady-state gradient Richardson number of $\text{Ri}_{\text{st}} = 0.25$, which is a result of the calibration procedure of the two-equation turbulence closure model (Burchard & Baumert, 1995; Umlauf & Burchard, 2005). The rotated stress vector $(\hat{\tau}^x, \hat{\tau}^y)$ and the eddy viscosity ν_t are compared to the analytical formulations from (A3) and (A4) in Fig. 6g,h, using the simulated surface stress and a mixed-layer depth diagnosed from the first zero-crossing of the simulated shear stress. For the shear stress the agreement is very good, but the parabolic analytical eddy viscosity overestimates the simulated profile by about one third, because it does not take into account effects of stratification that are present at the base of the plume. Still near the ice-ocean interface, the agreement between simulated and analytical eddy viscosity is very good, and both profiles converge to $\kappa(z' + z_0)$ near the interface. For the simulated profile, this is a consequence of the formulation of the Schmidt number in the ε -

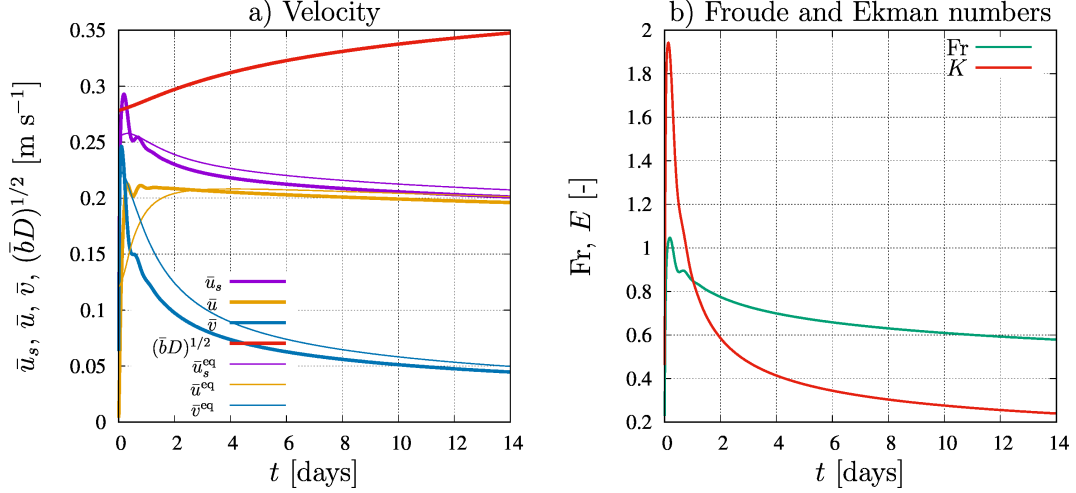


Figure 5. Time series of a) depth-averaged velocity diagnosed from GOTM and equilibrium velocity predicted by the steady-state theory presented in Appendix B as well as the phase velocity and b) Froude and Ekman numbers for the **def** scenario.

equation of the turbulence closure model (Burchard & Baumert, 1995; Umlauf & Burchard, 2005) for which the resulting ε -profile is shown in Fig. 6i.

4.2.2 Sensitivity to forcing parameters

In the default scenario described in Sec. 4.2.1, the entrainment velocity v_e is about 1 to 2 orders of magnitude larger than the melt velocity v_m , with peak values of v_e reaching almost 2 km y^{-1} , while the melt velocity has maximum values of about 20 m y^{-1} (magenta lines in Fig. 7). With that, the assumption of a rigid lid does not significantly influence the plume thickness. Highest entrainment and melt velocities are reached in the early adjustment phase of the plume due to maximum Froude and Ekman numbers (Fig. 5) after which a steady decrease is observed.

Increasing or decreasing the slope of the ice-ocean interface by a factor of 5 in the scenarios **ayp** and **aym**, has significant effects on the development of the plume. The steeper slope more than triples the final plume thickness to more than $D = 75 \text{ m}$, with entrainment velocities of up to $v_e = 20 \text{ km y}^{-1}$ and melt velocities of up to almost $v_m = 70 \text{ m y}^{-1}$ (Fig. 7a,d,g). In contrast, the scenario **aym** with the strongly decreased slope (Tab. 3), leads to on a very weak increase in plume thickness during the 14-day simulation, with entrainment velocities of about $v_e = 20 \text{ m y}^{-1}$ and melt velocities decreasing from initially $v_m = 10 \text{ m y}^{-1}$ to $v_m = 1 \text{ m y}^{-1}$ at the end of the simulation.

Also increasing (**z0p**) or decreasing (**z0m**) the roughness of the ice-ocean interface by an order of magnitude with respect to the default scenario has a measurable effect on the development of the plume (Fig. 7b,e,h). As shown by the equilibrium theory (Appendix B, Fig. B1), an increased roughness should lead to a decreased velocity but to an increased friction velocity. Since conditions for the equilibrium theory are met for the later stages of the plume development (Fig. 5a), plume velocity and friction velocity do show this behaviour here (not shown). With that, higher interfacial roughness leads to more turbulence inside the plume, and thus a higher entrainment velocity and a higher melt rate (Figs. 7e,h).

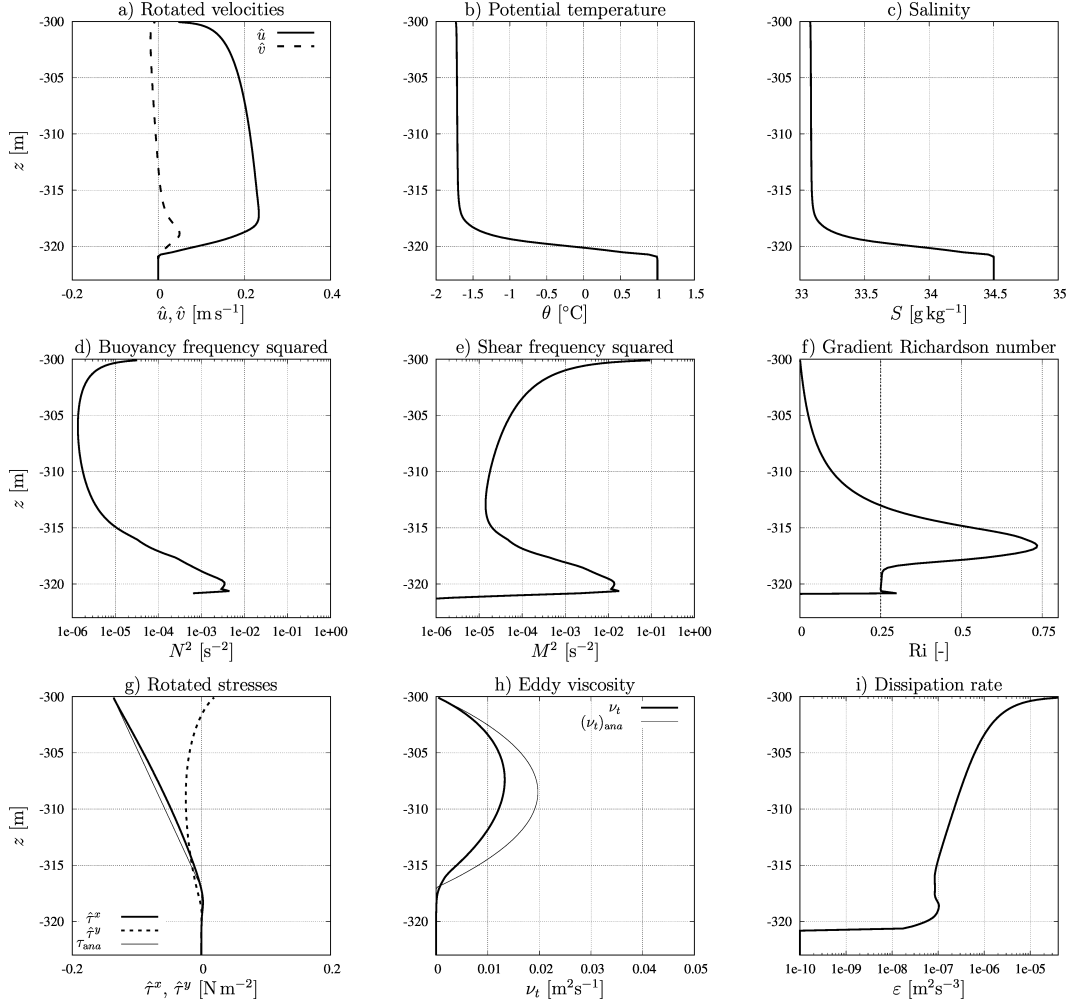


Figure 6. Profiles of a) rotated velocity, b) potential temperature, c) salinity, d) buoyancy frequency squared, e) shear frequency squared, f) gradient Richardson number, g) rotated stresses, h) eddy diffusivity, and i) dissipation rate for the **def** scenario at $t = 14$ days. In panels g) and h) the thin lines show analytical profiles based on the simulated surface stress and a mixed-layer depth diagnosed from the first zero-crossing of the simulated shear stress. In panel f) the dashed line indicates the steady-state Richardson number $Ri_{st} = 0.25$.

In contrast, changes in ambient potential temperature (scenarios **tap** and **tam**) have no significant impact on plume thickness and entrainment velocity (Figs. 7c,f). As expected, the melt rate increases by about 1.7 m y^{-1} for an increase of 1°C in ambient temperature (Fig. 7i).

4.2.3 Sensitivity to vertical resolution

To study the effect of coarser vertical resolution in three-dimensional numerical models, the water column of 150 m height is discretized with $k_{\max} = 50$ layers (10 layers over the upper 10 m) and $k_{\max} = 25$ layers (5 layers over the upper 10 m) instead of $k_{\max} = 500$ layers (38 layers over the upper 10 m). Such coarser resolutions are in the order of what three-dimensional models of ice-cavities using surface-following coordinates can typically afford. Given the fact that the initial plume thickness of $D = 5 \text{ m}$ is re-

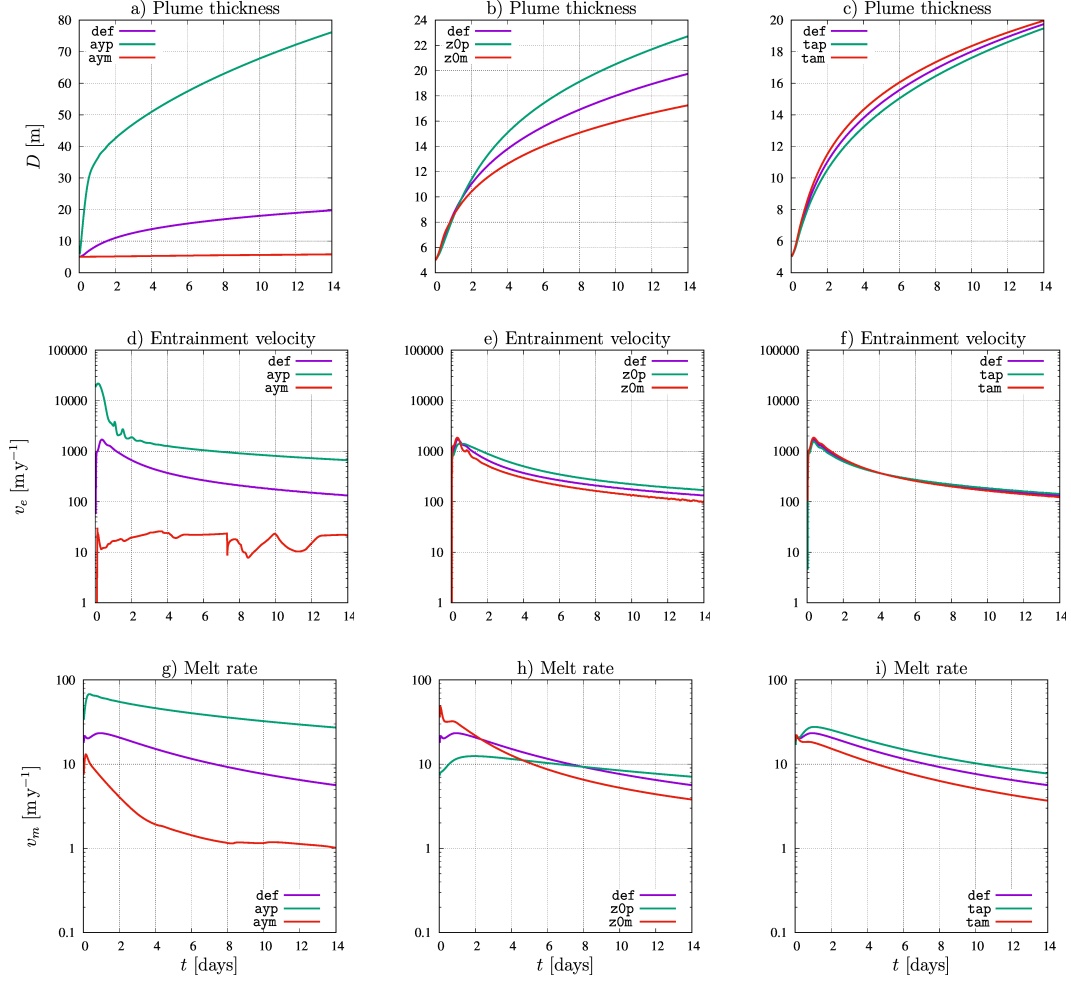


Figure 7. Time series of plume thickness D (panels a, b, c), entrainment velocity v_e (panels d, e, f) and melt rate v_m (panels g, h, i), comparing results of the default scenario **def** with sensitivity simulations **ayp** and **aym** for interfacial slope (panels a, d, g), **z0p** and **z0m** for interfacial roughness (panels b, e, h) and **tap** and **tam** for ambient temperature (panels c, f, i).

solved by only a few discrete values, it is already quite coarse. The resulting vertical profiles (Fig. 8) for $k_{\max} = 500$, $k_{\max} = 50$ and $k_{\max} = 25$ layers show that the coarse resolution simulations reproduce the high-resolution profiles with sufficient accuracy. Velocity, potential temperature and salinity profiles (Fig. 8a-c) are reproduced very accurately, due to the largely resolution-independent ocean-to-ice flux parameterization (Sec. 3.1 and 3.2). Buoyancy frequency squared N^2 and shear frequency squared M^2 and thus the gradient Richardson number (Figs. 8d-f) are well reproduced at the ice-ocean interface and in the plume interior, but at the plume base, the sharp peaks of N^2 and M^2 are not properly resolved. For the coarse resolution with $k_{\max} = 25$ layers, the gradient Richardson number does not yield a value of $\text{Ri}_{\text{st}} = 0.25$ inside the entrainment layer.

Resulting plume thickness, entrainment velocity and melt rate are shown for all three vertical resolutions in Fig. 9. It can be seen that for $k_{\max} = 50$ layers the development of the plume thickness is still accurately reproduced with a maximum error of about 1 m (Fig. 9a). For $k_{\max} = 25$ layers, due to the resolution of the initial plume thickness with only a few model layers, there is an overall underestimation of the plume thickness by

about 3 m, which is however not significantly increasing during the simulation. After some deviations in the initial phase, also entrainment velocity and melt velocity are well-reproduced by both coarse resolution simulations (Fig. 9b,c).

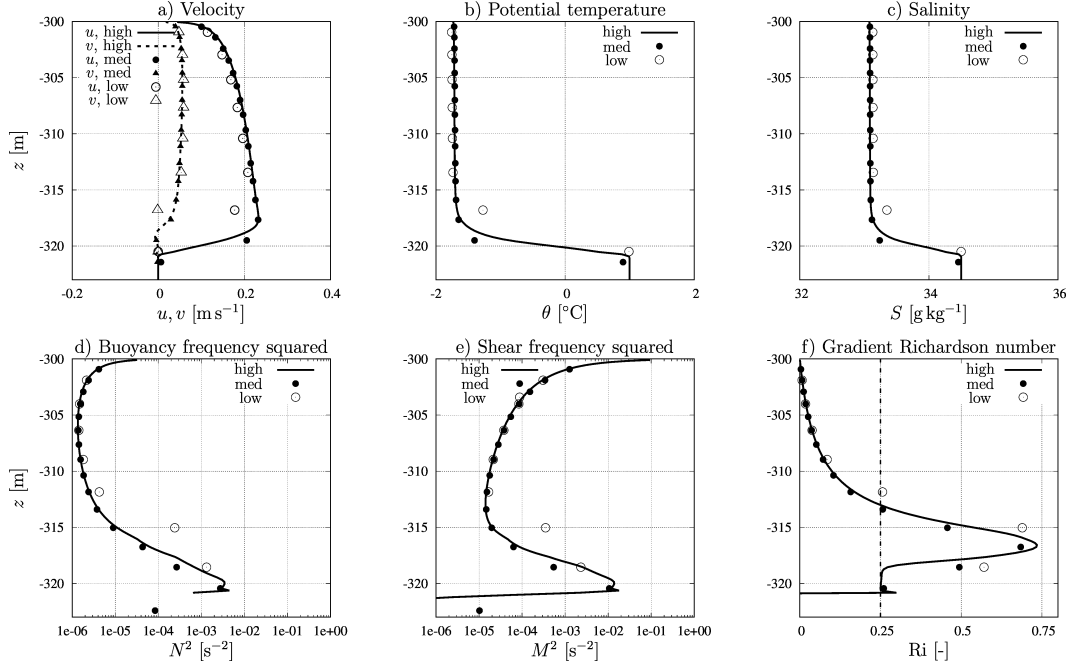


Figure 8. Vertical profiles of a) velocity, b) potential temperature, c) salinity, d) buoyancy frequency squared, e) shear frequency squared and f) gradient Richardson number after 14 days of simulation using the default scenario with high resolution of $k_{\max} = 500$ layers (lines), a medium resolution of $k_{\max} = 50$ layers (black symbols) and a low resolution of $k_{\max} = 25$ layers (open symbols).

792

4.3 Comparison to entrainment parameterisations

793

794

795

796

797

798

799

800

801

802

Entrainment is the process of turbulent transport of relatively stagnant ambient water into the turbulent plume layer through its base with the consequence of an increase in plume thickness and density. Despite its complex hydrodynamics in a region of sharp vertical gradients, various parameterizations for the entrainment process have been successfully developed. Moreover, computationally efficient vertically integrated models of subglacial plumes have become a common tool in investigating subglacial melt processes in ice cavities (Jenkins, 1991; P. R. Holland & Feltham, 2006; Hewitt, 2020). Here, we first introduce these parameterizations and then compare their performance to the results of the vertically resolved model for the default scenario and the six sensitivity scenarios.

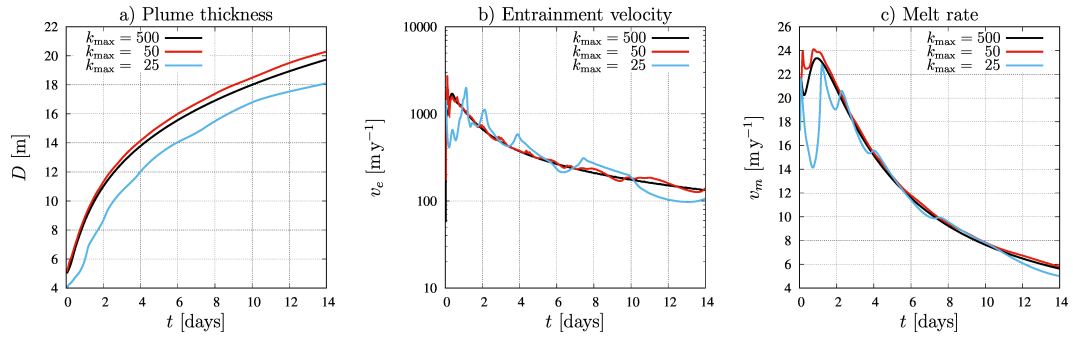


Figure 9. Analysed plume thickness D (panel a), entrainment velocity v_e (panel b) and melt rate v_m (panel c) for the default scenario for three different vertical resolutions during 14 days of simulation. Three different vertical resolutions were applied, $k_{\max} = 500$ layers, $k_{\max} = 40$ layers and $k_{\max} = 20$ layers.

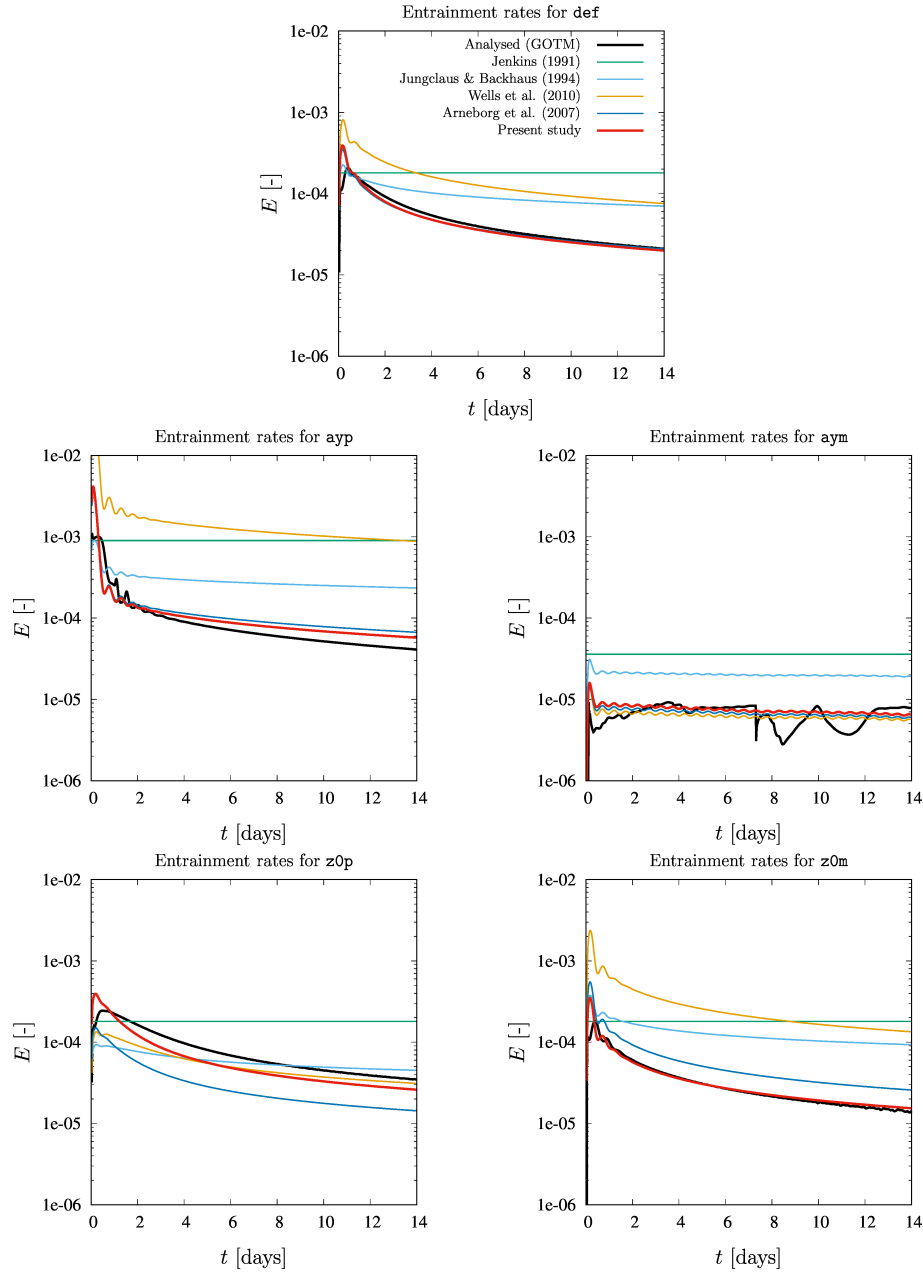


Figure 10. Entrainment rates analysed by GOTM and parameterized by five different entrainment models for the default scenario and the **ayp**, **aym**, **z0p** and **z0m** scenarios. The results for **tap** and **tam** are very similar to those of **def** and are therefore not shown here.

The entrainment velocity v_e is defined as the rate of plume thickening due to entrainment of ambient water across the plume base. For the parameterisation of the non-dimensional entrainment rate $E = v_e/\bar{u}_s$, various formulations have been proposed, of which we are comparing the following five to the vertically resolved entrainment:

1. A constant entrainment rate has been proposed by Jenkins (1991):

$$E = E_0 \sin \alpha \quad (61)$$

with $E_0 = 0.036$.

2. The entrainment model by Jungclaus and Backhaus (1994) calculates the entrainment rate as

$$E = \frac{c_L^2}{S_m} \sqrt{1 + \frac{\text{Ri}_b}{S_m}}, \quad (62)$$

with the constant empirical parameter $c_L = 0.0275$ and the turbulent Schmidt number

$$S_m = \frac{\text{Ri}_b}{0.725 \left(\text{Ri}_b + 0.186 - \sqrt{\text{Ri}_b^2 - 0.316 \text{Ri}_b + 0.0364} \right)}. \quad (63)$$

The present simulations with this modified version showed a substantial underestimation of entrainment rates in comparison to other formulations and to the vertically resolved plume model, such that we retained the original value that Jungclaus and Backhaus (1994) adopted from Kochergin (1987).

3. For subcritical flow, Wells et al. (2010) proposed an entrainment rate

$$E = \frac{1}{8} \frac{\bar{\Gamma}}{\cos \alpha} \text{Fr}^4 \left(\frac{D}{l_h} \right)^3 \quad (64)$$

that depends on the Froude number Fr , with the bulk mixing coefficient $\bar{\Gamma} = 0.2$, and $0.1 < D/l_h < 0.3$ with the characteristic horizontal turbulent length scale l_h .

4. The entrainment rate proposed by Arneborg et al. (2007),

$$E = a C_d \text{Fr}^b K^c, \quad (65)$$

with $a = 0.084$, $b = 2.65$, $c = 0.6$ and a constant drag coefficient $C_d = 0.0025$ depends on the Ekman number K , additionally.

5. We finally recalibrate the approach by Arneborg et al. (2007) which has been optimized for dense bottom currents in the Baltic Sea using a constant drag coefficient C_d :

$$E = \hat{a} c_d \text{Fr}^{\hat{b}} K^{\hat{c}}, \quad (66)$$

including now the depth and roughness dependent drag coefficient c_d defined in (44), using the plume thickness d instead of the upper layer thickness $h_{k_{\max}}$. By reformulating (66) as

$$\ln \left(\frac{E}{c_d} \right) = \ln(\hat{a}) + \hat{b} \ln(\text{Fr}) + \hat{c} \ln(K), \quad (67)$$

and formulating the mean-square error between diagnosed and predicted e/c_d as

$$f(\hat{a}', \hat{b}, \hat{c}) = \frac{1}{i_{\max}} \sum_{i=1}^{i_{\max}} \left(\hat{a}' + \hat{b} \ln(\text{Fr}_i) + \hat{c} \ln(K_i) - \ln \left(\frac{E_i}{(c_d)_i} \right) \right)^2, \quad (68)$$

with $\hat{a}' = \ln(\hat{a})$, where E_i , $(c_d)_i$, Fr_i and K_i are diagnosed values for all experiments and all time steps, a least-square method with $\partial f / \partial \hat{a}' = \partial f / \partial \hat{b} = \partial f / \partial \hat{c} = 0$ gives an optimal parameter set $(\hat{a}, \hat{b}, \hat{c})$ with a minimum error. The resulting values ($\hat{a} = 0.052$, $\hat{b} = 2.56$ and $\hat{c} = 0.29$) are similar to the original values by

Arneborg et al. (2007), but with a significantly smaller influence of the Ekman number which includes the variable roughness parameter c_d . This model will be denoted as *Present study* in Fig. 10.

As already shown in Fig. 7, the entrainment velocity can vary over several orders of magnitude across the different scenarios. In Fig. 10, we compare the non-dimensional entrainment rates diagnosed from the vertically resolved plume simulations with the values predicted by the five plume parameterisations given above. The results differ substantially. For some scenarios, the constant entrainment rate by Jenkins (1991) reproduces correctly the order of magnitude of the diagnosed entrainment, but obviously not its temporal evolution also during later balanced states of the plume. The scenarios including variations of the slope angle, \mathbf{a}_{yp} and \mathbf{a}_{ym} , show that the concept of formulating the entrainment rate as function of the slope angle in this simple parameterization roughly reproduces the correct order of magnitude of the entrainment process. The bulk Richardson number dependent parameterisation by Jungclaus and Backhaus (1994) does largely follow the decreasing trends of the entrainment rate, but is for most scenarios generally significantly overestimating or underestimating the magnitude, a performance that is also seen for the parameterization by Wells et al. (2010) which is based on the fourth power of the Froude number. The performance of the Froude and Ekman number dependent parameterization by Arneborg et al. (2007) is generally better than those previously discussed, and its accuracy could be strongly improved by the recalibration to the present seven scenarios. Therefore, the good performance of the original Arneborg et al. (2007) calibration and the optimal performance of the newly calibrated formulation is not a surprise. This is also because the Arneborg et al. (2007) calibration used the same turbulence closure model as the present study. But the design of this parameterization depending on two non-dimensional plume parameters, Fr and K , that vary independently (see Fig. 5) seems to be the most promising for rotational plumes.

5 Discussion

The discussion of the results of this study will concentrate on four issues that might be of interest for future modeling of ice shelves: the benefits of the analytical solution (Sec. 5.1), the implications of the numerical analysis (Sec 5.2), the consequences of the vertical plume structure and resulting entrainment of ambient water (Sec. 5.3) and the remaining uncertainties in modeling of subglacial plumes and melt rates (Sec. 5.4).

5.1 Analytical solution

The analytical solution for the vertical profiles of velocity, temperature and salinity of subglacial plumes that is presented as Eqs. (33) - (35) is based on a number of simplifying assumptions: neglect of Earth rotation, vertically homogeneous acceleration of the plume, parabolic eddy viscosity and diffusivity, and stationarity. Despite its idealized character, the solution can be used for a number of purposes:

1. It can be used as a simple test bed for melt flux parameterizations that is not affected by numerical uncertainties. Despite the high degree of simplification, realistic values for melt rates and ocean-to-ice heat fluxes were calculated (Sec. 2.5.3). The analytical solution also shows the high degree of vertical homogeneity of the profiles of temperature and salinity and the significant differences between boundary and melt-layer values of temperature and salinity, due to the high Schmidt numbers (Fig. 2). Also, entrainment fluxes can be quantitatively compared to melt fluxes.
2. The analytical solution is a basis to construct consistent and convergent formulations for the discrete melt layer fluxes (Sec. 3.1 and 3.2).
3. Finally, the analytical solution allows for the analysis of numerical convergence for vertically resolving plume models (Sec. 3.4).

5.2 Numerical accuracy

The convergence analysis of a numerical plume model towards the analytical solution (Sec. 3.4) shows that ocean-to-ice fluxes and consequently melt rates can accurately be calculated also with a relatively coarse vertical resolution near the ice-ocean interface. The major requirement to achieve this is the proper discretization of the ocean-to-ice momentum flux. Using a drag coefficient that is independent of the upper-layer thickness leads to highly inaccurate and divergent results, due to the strong velocity gradients near the interface. In contrast, discrete tracer flux formulations that are independent of the upper-layer thickness are numerically inconsistent. Still, they do not lead to a measurable loss of accuracy when the vertical tracer profiles are quasi-homogeneous.

Vertical resolution does however matter for the numerical reproduction of the entrainment process at the base of the plume, where strong vertical gradients are present. A typical vertical extent of the entrainment layer is of the order of 2 - 4 m (Fig. 6). Although second-moment turbulence closure schemes are relatively robust with respect to vertical resolution (Umlauf & Burchard, 2005; Li et al., 2021), vertical grid resolutions should be of the order of 2 m or higher in the region of the entrainment layer. This is demonstrated in Fig. 8 where an entrainment-layer resolution of about 1.5 m still properly reproduces the vertical plume structure of a high-resolution model at the end of a two-week simulation. Also entrainment velocity and melt rates are sufficiently reproduced by this resolution, but for a resolution of 3 m, results start deteriorating (Fig. 9). For typical plume thicknesses of the order of 10 m, this means that more than 5 numerical layers should be present in the plume region. For geopotential coordinates, this might mean an overall vertical resolution of 2 m at all depths where the ice-ocean interface is present, i.e., typically several 100 m below the undisturbed mean sea level. Also for terrain-following coordinates (where vertical resolution decreases with water depth) such resolutions are still quite a challenge. Here, vertically adaptive coordinates (Hofmeister et al., 2010; Gräwe et al., 2015) may be the solution, since they allow concentrating the resolution at sharp density interfaces such as in the entrainment layer. This principle has been used by Umlauf et al. (2010) for the simulation of channelized dense bottom currents and could also be applied to subglacial plume simulations.

5.3 Vertical plume structure and entrainment

The vertical structure of subglacial plumes is believed to resemble that of dense bottom currents, turned upside down (Jenkins, 2016). That explains why often model tools are applied to subglacial plumes that have been developed for dense bottom currents and oceanic overflows. In both cases, determining entrainment rates is important. For oceanic overflows, the entrainment rates determine their potential for ventilating the deep ocean, for subglacial plumes they determine the transport of relatively warm and salty ambient water towards the ice-ocean interface and therefore play an importance role in setting the melt rate. The fundamental dynamical difference between dense bottom currents and subglacial plumes is the additional (stabilizing) interfacial buoyancy flux due to melt processes at the ice-ocean interface of subglacial plumes that ultimately drives the flow.

Entrainment velocities analyzed from the present models results are within the range of common entrainment parameterizations typically used in vertically integrated plume models of subglacial plumes (Fig. 10). Those parameterizations however lead to very different estimates of entrainment rates. To provide a robust and reliable entrainment parameterization, the formulation by Arneborg et al. (2007) has been re-calibrated for a depth-dependent drag coefficient (66) and shows an agreeable accuracy over a large range of plume parameters.

5.4 Remaining uncertainties

The vertical structure of dense bottom currents has been well-observed in the ocean, e.g. the Faroe Bank Channel overflow (Fer et al., 2010) and overflows into the Baltic Sea (Umlauf et al., 2007). Such high-resolution observations of subglacial plumes are not available due to the thickness of the glacial ice cover and the large surface area of the floating ice tongues. The few available observations (e.g., Washam et al., 2020), do not provide sufficient resolution and coverage of the entire plume thickness. It can therefore only be assumed by analogy how subglacial plumes are vertically structured. In agreement with observations and models of dense overflows in the Western Baltic Sea (Arneborg et al., 2007; Umlauf et al., 2007, 2010) with similar characteristics in terms of similarity parameters such as the Froude and Ekman numbers, the interior of subglacial plumes can be assumed to be well-mixed and the plumes can be assumed to be bounded by sharp density interfaces in the entrainment layer. However, the uncertainties about the vertical structure of subglacial plumes can only be reduced by very challenging in-situ field observations under glacial ice tongues.

Moreover, the underlying assumption for one-dimensional water column models of a plume that is laterally homogeneous along the ice-ocean interface is highly idealized and unrealistic. The ice-ocean interface may be smooth on the small scale, but it is plausible to assume non-negligible sub-grid scale roughness that exerts a form drag on the flow. This drag needs to be parameterized in coarse ocean models via an effectively roughness length k_s (Sec. 2.4). Our model experiments show that the roughness length has a large influence on plume thickness, entrainment velocity and melt rate (Fig. 10). Since the determination of this effective roughness is highly uncertain, sensitivity studies with respect to this parameter are recommended.

The biggest uncertainty however remains for the detailed structure of the topography of the ice-ocean interface and the effects on the plume dynamics. Subglacial plumes are often thought of as wide layers of buoyant water propagating across ice tongues with relatively plain subglacial topographies (P. R. Holland & Feltham, 2006). It is however known that plumes occur as highly channelized flows, similar to overflows in the ocean (Umlauf et al., 2007; Fer et al., 2010), but probably occurring on even smaller scales (Rignot & Steffen, 2008; Washam et al., 2020). To investigate the impact of these topographically highly diverse plume dynamics on the net basal melt rate, detailed studies of more dimensional flows need to be carried out such as cross-sections models of channelized subglacial plumes, similar to the two-dimensional model of dense bottom currents presented by Umlauf et al. (2010).

6 Conclusions

A numerical one-dimensional water column model of subglacial plumes has been presented here that should help to constrain ocean models of ice shelves. To our knowledge this is the first high-resolution one-dimensional model that couples the physics of the melt layer to second-moment turbulence closures inside the plume and across the entrainment layer. This modeling strategy allows for quantitative predictions of entrainment processes of ambient water into the plume, such that it can serve as a benchmark for models with simpler physics such as bulk entrainment models.

Using an analytical solution of the plume, accurate and convergent numerical expressions for fluxes across the ice-ocean interface are formulated. Specifically, they do also reproduce these fluxes accurately for relatively coarse near-interface resolution. The probably most critical finding is that the vertical model resolution in the region of the entrainment layer should ideally be order of 2 - 3 m, which provides a challenge to existing ocean models for ice shelves. Future efforts should be directed at developing flex-

ible numerical schemes that allow this locally high resolution also in large scale ocean models.

Appendix A Derivation of the analytical solution

A1 Velocity profile

Under the conditions discussed in Sec. 2.1, and ignoring Earth rotation, the momentum budget (7) within the plume has the following form:

$$\partial_t u - \partial_{z'} (\nu_t \partial_{z'} u) = b \tan \alpha, \quad (\text{A1})$$

with the boundary conditions

$$\nu_t \partial_{z'} u = \begin{cases} (u_*^b)^2 & \text{for } z' = 0, \\ u_*^s |u_*^s| & \text{for } z' = D, \end{cases} \quad (\text{A2})$$

where u_*^s is the friction velocity in the entrainment layer at the base of the plume. Assuming stationarity of the velocity profile and combining (A1) and (A2), a linear stress profile is resulting:

$$\nu_t \partial_{z'} u = (u_*^b)^2 \frac{D - z'}{D} + u_*^s |u_*^s| \frac{z'}{D}. \quad (\text{A3})$$

The parabolic profile of eddy viscosity is given as

$$\nu_t = \kappa u_*^b (z' + z_0) \frac{D - z'}{D}, \quad (\text{A4})$$

see Burchard and Hetland (2010), where for small z' (18) is retained. Combining (A3) and (A4) gives

$$\partial_{z'} u = \frac{u_*^b}{\kappa} \frac{1}{z' + z_0} + \frac{u_*^s |u_*^s|}{\kappa u_*^b} \frac{z'}{(z' + z_0)(D - z')}. \quad (\text{A5})$$

Integrating (A5) from 0 to z' and using

$$\frac{1}{z' + z_0} + \frac{1}{D - z'} = \frac{D + z_0}{(z' + z_0)(D - z')} \quad (\text{A6})$$

results in

$$u(z') = \frac{u_*^b}{\kappa} \ln \left[\frac{z' + z_0}{z_0} \right] - \frac{u_*^s |u_*^s|}{\kappa u_*^b} \left(\frac{z_0}{D + z_0} \ln \left[\frac{z' + z_0}{z_0} \right] + \frac{D}{D + z_0} \ln \left[\frac{D - z'}{D} \right] \right). \quad (\text{A7})$$

The plume-averaged velocity

$$\bar{u} = \frac{1}{D} \int_0^D u(z') dz', \quad (\text{A8})$$

results from vertical averaging of (A7) as

$$\bar{u} = \frac{u_*^b}{\kappa} A - \frac{u_*^s |u_*^s|}{\kappa u_*^b} \left(\frac{z_0}{D + z_0} A - \frac{D}{D + z_0} \right) \quad (\text{A9})$$

with the integration constant

$$A = \frac{1}{D} \int_0^D \ln \left[\frac{z' + z_0}{z_0} \right] dz' = \frac{D + z_0}{D} \ln \left[\frac{D + z_0}{z_0} \right] - 1. \quad (\text{A10})$$

Combining (A7) and (A9) finally gives the velocity profile fulfilling a prescribed depth-averaged velocity \bar{u} , see (33).

1020 **A2 Tracer profile**

1021 Let c be a tracer obeying the following one-dimensional budget equation:

$$1022 \quad \partial_t c + \partial_z f^c = 0, \quad (\text{A11})$$

1023 with the upward turbulent tracer flux,

$$1024 \quad f^c = -\nu'_t \partial_z c = \nu'_t \partial_{z'} c, \quad (\text{A12})$$

1025 the ice-ocean interface value

$$1026 \quad c(z_b - [z_0^c - z_0]) = c_b, \quad (\text{A13})$$

1027 where the location of the boundary value for c at the ice-ocean interface is slightly shifted
1028 with respect to the no-slip boundary condition for velocity (see Sec. 2.1, 2.2 and 2.4).

1029 As flux boundary conditions, we define

$$1030 \quad f^c = \begin{cases} f_b^c & \text{for } z' = 0, \\ f_s^c & \text{for } z' = D. \end{cases} \quad (\text{A14})$$

1031 An eddy diffusivity profile is constructed by dividing the parabolic eddy viscosity
1032 profile (A4) by the the turbulent Prandtl number Pr_t :

$$1033 \quad \nu'_t = \frac{\kappa}{\text{Pr}_t} |u_*^b| (z' + z_0) \frac{D - z'}{D}, \quad (\text{A15})$$

1034 Assuming that $\partial_t c$ is independent of z , the tracer flux will have the following linear pro-
1035 file:

$$1036 \quad f^c = \nu'_t \partial_{z'} c = f_b^c \frac{D - z'}{D} + f_s^c \frac{z'}{D}. \quad (\text{A16})$$

1037 Combining (A11) and (A16) gives the rate of change of c :

$$1038 \quad \partial_t c = \frac{f_s^c - f_b^c}{D}, \quad (\text{A17})$$

1039 such that the original tracer equation (A11) can be reformulated as

$$1040 \quad \partial_z f^c = -\partial_{z'} f^c = -\frac{f_s^c - f_b^c}{D}. \quad (\text{A18})$$

1041 Combining (A15) and (A16), we obtain

$$1042 \quad \partial_{z'} c = \frac{\text{Pr}_t f_b^c}{\kappa |u_*^b|} (z' + z_0)^{-1} + \frac{\text{Pr}_t f_s^c}{\kappa |u_*^b|} \frac{z'}{(z' + z_0)(D - z')}. \quad (\text{A19})$$

1043 Using (A6) and integrating (A19) from $z_0^c - z_0$ to z' with (A13) reads as

$$\begin{aligned} c(z') - c_b &= \frac{\text{Pr}_t f_b^c}{\kappa |u_*^b|} \ln \left[\frac{z' + z_0}{z_0^c} \right] \\ &\quad - \frac{\text{Pr}_t f_s^c}{\kappa |u_*^b|} \left(\frac{z_0}{D + z_0} \ln \left[\frac{z' + z_0}{z_0^c} \right] + \frac{D}{D + z_0} \ln \left[\frac{D - z'}{D + z_0 - z_0^c} \right] \right) \\ &= \frac{\text{Pr}_t f_b^c}{\kappa |u_*^b|} \left(\ln \left[\frac{z' + z_0}{z_0} \right] + \frac{\kappa}{\text{Pr}_t} \beta^c \right) \\ &\quad - \frac{\text{Pr}_t f_s^c}{\kappa |u_*^b|} \left(\frac{z_0}{D + z_0} \left(\ln \left[\frac{z' + z_0}{z_0} \right] + \frac{\kappa}{\text{Pr}_t} \beta^c \right) \right. \\ &\quad \left. + \frac{D}{D + z_0} \ln \left[\frac{D - z'}{D + z_0 \left(1 - \exp \left[-\frac{\kappa}{\text{Pr}_t} \beta^c \right] \right)} \right] \right) \end{aligned} \quad (\text{A20})$$

1045 with β^c from (31). Vertical averaging of (A20) gives

$$\begin{aligned}
 \bar{c} - c_b &= \frac{\text{Pr}_t f_b^c}{\kappa |u_*^b|} A_c - \frac{\text{Pr}_t f_s^c}{\kappa |u_*^b|} \left(\frac{z_0}{D + z_0} A_c - \frac{D}{D + z_0} \left(1 - \ln \left[\frac{D}{D + z_0 - z_0^c} \right] \right) \right) \\
 &= \frac{\text{Pr}_t f_b^c}{\kappa |u_*^b|} A_c - \frac{\text{Pr}_t f_s^c}{\kappa |u_*^b|} \left(\frac{z_0}{D + z_0} A_c - \right. \\
 &\quad \left. \frac{D}{D + z_0} \left(1 - \ln \left[\frac{D}{D + z_0 \left(1 - \exp \left[-\frac{\kappa}{\text{Pr}_t} \beta^c \right] \right)} \right] \right) \right)
 \end{aligned} \tag{A21}$$

1047 with the vertically averaged tracer concentration \bar{c} and the integration constant

$$\begin{aligned}
 A_c &= \frac{1}{D} \int_0^D \ln \left[\frac{z' + z_0}{z_0^c} \right] dz' = \frac{D + z_0}{D} \ln \left[\frac{D + z_0}{z_0} \right] - \left(1 - \ln \left[\frac{z_0}{z_0^c} \right] \right) \\
 &= \frac{D + z_0}{D} \ln \left[\frac{D + z_0}{z_0} \right] - \left(1 - \frac{\kappa}{\text{Pr}_t} \beta^c \right).
 \end{aligned} \tag{A22}$$

1049 In (A20) - (A22), the formulations including β^c instead of z_0^c , using (30), are those that
 1050 should be used for computations, since z_0^c is typically so small that calculations of its re-
 1051 reciprocal would result in overflows. Combining (A20) and (A21) leads to a tracer profile
 1052 based on the depth mean tracer concentration \bar{c} instead of the melt layer tracer concen-
 1053 tration c_b .

1054 Appendix B Equilibrium dynamics in plume

1055 The depth-averaged bulk dynamics in a well-adjusted plume can approximately be
 1056 described by a steady-state condition for the momentum equations

$$\begin{aligned}
 d_t(\bar{u}D) &= -c_d \bar{u} \bar{u}_s & + \bar{b}D \sin \alpha_x + f \bar{v}D, \\
 d_t(\bar{v}D) &= -c_d \bar{v} \bar{u}_s & + \bar{b}D \sin \alpha_y - f \bar{u}D,
 \end{aligned} \tag{B1}$$

1058 as formulated by (Jenkins, 1991). For a slope aligned with the y -direction ($\alpha_x = 0$) the
 1059 following balance results (Arneborg et al., 2007):

$$\begin{aligned}
 -c_d \bar{u}^{\text{eq}} ((\bar{u}^{\text{eq}})^2 + (\bar{v}^{\text{eq}})^2)^{1/2} &+ f \bar{v}^{\text{eq}} D = 0, \\
 -c_d \bar{v}^{\text{eq}} ((\bar{u}^{\text{eq}})^2 + (\bar{v}^{\text{eq}})^2)^{1/2} &+ \bar{b}D \sin \alpha_y - f \bar{u}^{\text{eq}} D = 0,
 \end{aligned} \tag{B2}$$

1061 with the equilibrium velocity vector $(\bar{u}^{\text{eq}}, \bar{v}^{\text{eq}})$. After introducing the non-dimensional
 1062 variables

$$\tilde{u} = \frac{\bar{u}^{\text{eq}}}{fD}; \quad \tilde{v} = \frac{\bar{v}^{\text{eq}}}{fD}; \quad \tilde{u}_s = (\tilde{u}^2 + \tilde{v}^2)^{1/2}; \quad \tilde{b} = \frac{\bar{b}}{f^2 D}; \quad \tilde{u}_*^b = \frac{u_*}{fD} = c_d^{1/2} \tilde{u}_s, \tag{B3}$$

1064 (B2) can be formulated as follows:

$$\begin{aligned}
 -c_d \tilde{u} \tilde{u}_s &= -\tilde{v} \\
 -c_d \tilde{v} \tilde{u}_s &+ \tilde{b} \sin \alpha_y = \tilde{u}
 \end{aligned} \tag{B4}$$

1066 Multiplying the first equation in (B4) by \tilde{u} and the second equation by \tilde{v} and subsequently
 1067 adding the results gives

$$-c_d \tilde{u}_s^3 = -\tilde{b} \tilde{v} \sin \alpha_y. \tag{B5}$$

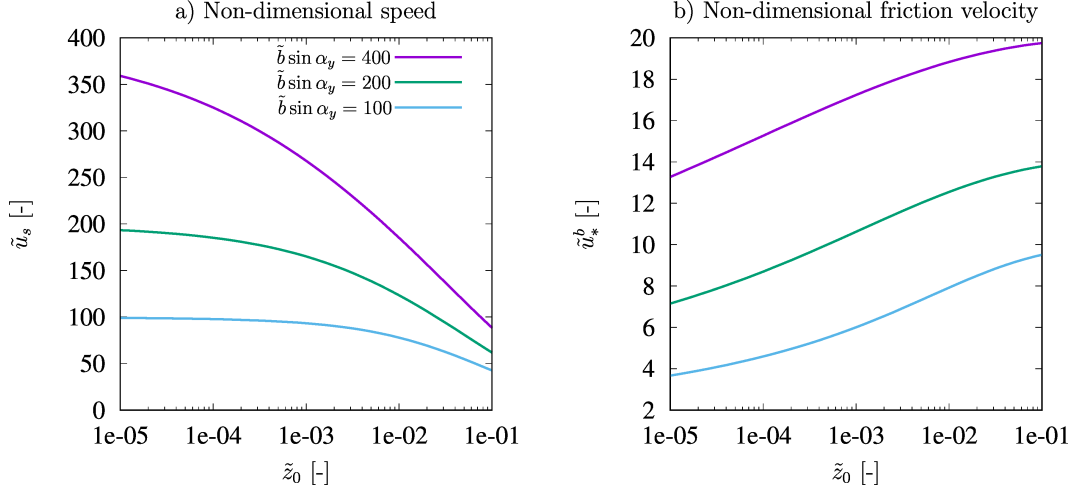


Figure B1. Non-dimensional speed \tilde{u}_s (panel a) and friction velocity \tilde{u}_*^b (panel b) as function of the non-dimensional roughness \tilde{z}_0 for three different values of $\tilde{b} \sin \alpha_y$. For a density difference of $\Delta\rho = 4 \text{ kg m}^{-3}$ between ambient water and plume water, an interfacial slope of $\tan \alpha_y = 10^{-3}$ and a latitude of 79°N , the values $\tilde{b} \sin \alpha_y = (400, 200, 100)$ correspond to plume thicknesses of $D = (25\text{m}, 12.5\text{m}, 6.25\text{m})$.

Multiplying the first equation in (B4) by \tilde{v} and the second equation by \tilde{u} and subsequently subtracting the results gives

$$\tilde{u}_s^2 = \tilde{b} \tilde{u} \sin \alpha_y. \quad (\text{B6})$$

Squaring (B5) and (B6), adding the results and rearranging gives

$$\tilde{u}_s^4 + \frac{1}{c_d^2} \tilde{u}_s^2 - \frac{\tilde{b}^2 \sin^2 \alpha_y}{c_d^2} = 0, \quad (\text{B7})$$

which results in

$$\tilde{u}_s^2 = -\frac{1}{2c_d^2} + \sqrt{\frac{1}{4c_d^4} + \frac{\tilde{b}^2 \sin^2 \alpha_y}{c_d^2}} \quad (\text{B8})$$

and consequently

$$(\tilde{u}_*^b)^2 = -\frac{1}{2c_d} + \sqrt{\frac{1}{4c_d^2} + \tilde{b}^2 \sin^2 \alpha_y}. \quad (\text{B9})$$

The velocity components \tilde{u} and \tilde{v} can be calculated by means of (B5) and (B6).

The dependence of the non-dimensional current speed \tilde{u}_s and the non-dimensional friction velocity $\tilde{u}_*^b = c_d^{1/2} \tilde{u}_s$ on the non-dimensional interfacial roughness is shown in Fig. B1 for three different values of the non-dimensional buoyancy forcing $\tilde{b} \sin \alpha_y$. Expectedly, a larger roughness length leads to a decreased plume velocity, however, it leads to an increased friction velocity indicating a more turbulent plume. This can be explained by the fact that the decrease of current speed due to increased roughness \tilde{z}_0 is smaller than the corresponding increase in $c_d^{1/2}$. This non-linear effect is not reproduced by models that use a constant drag coefficient.

Acknowledgments

The work of this study has been supported by the collaborative project GROCE (Greenland Ice Sheet Ocean Interaction) funded by the German Federal Ministry of Research

and Education under the grant no. 03F0855E. The implementation of the additional subglacial plume processes has been financially supported by the Leibniz Institute of Baltic Sea Research Warnemünde through a contract with Bolding & Bruggeman ApS in Denmark. Much of the work for this study by Hans Burchard have been carried out during a sabbatical visit at the Scottish Association of Marine Science in Oban (Scotland). The authors are grateful for the constructive comments by Knut Klingbeil (Warnemünde, Germany) on earlier versions of the manuscript.

Software Availability Statement: The source on which this study is based can be accessed here: <https://github.com/gotm-model/code/tree/plume>. The ice module can be found here:

https://github.com/BoldingBruggeman/stim/tree/bafl/src/models/basal_melt. Setup and output for the default scenario are provided at <https://github.com/gotm-model/cases/tree/master/plume>. Note to reviewers of this submission: For the final manuscript version, a link to zenodo will be provided instead.

References

- Absi, R. (2021). Reinvestigating the parabolic-shaped eddy viscosity profile for free surface flows. *Hydrology*, 8(3), 126.
- Arneborg, L., Fiekas, V., Umlauf, L., & Burchard, H. (2007). Gravity current dynamics and entrainment - A process study based on observations in the Arkona Basin. *J. Phys. Oceanogr.*, 37(8), 2094–2113.
- Burchard, H., & Baumert, H. (1995). On the performance of a mixed-layer model based on the κ - ϵ turbulence closure. *J. Geophys. Res.*, 100(C5), 8523–8540.
- Burchard, H., & Bolding, K. (2001). Comparative analysis of four second-moment turbulence closure models for the oceanic mixed layer. *J. Phys. Oceanogr.*, 31(8), 1943–1968.
- Burchard, H., & Hetland, R. D. (2010). Quantifying the contributions of tidal straining and gravitational circulation to residual circulation in periodically stratified tidal estuaries. *J. Phys. Oceanogr.*, 40, 1243–1262.
- Burchard, H., & Petersen, O. (1999). Models of turbulence in the marine environment - A comparative study of two-equation turbulence models. *J. Mar. Syst.*, 21(1-4), 29–53.
- Burchard, H., Schuttelaars, H. M., & Geyer, W. R. (2013). Residual sediment fluxes in weakly-to-periodically stratified estuaries and tidal inlets. *J. Phys. Oceanogr.*, 43(9), 1841–1861.
- Cheng, C., Jenkins, A., Wang, Z., & Liu, C. (2020). Modeling the vertical structure of the ice shelf–ocean boundary current under supercooled condition with suspended frazil ice processes: A case study underneath the Amery Ice Shelf, East Antarctica. *Ocean Modell.*, 156, 101712.
- Cheng, Y., Canuto, V., & Howard, A. (2002). An improved model for the turbulent pbl. *J. Atmos. Sci.*, 59(9), 1550–1565.
- Church, J. A., White, N. J., Konikow, L. F., Domingues, C. M., Cogley, J. G., Rignot, E., ... Velicogna, I. (2011). Revisiting the Earth’s sea-level and energy budgets from 1961 to 2008. *Geophys. Res. Lett.*, 38(18).
- Dansereau, V., Heimbach, P., & Losch, M. (2014). Simulation of subice shelf melt rates in a general circulation model: Velocity-dependent transfer and the role of friction. *J. Geophys. Res.*, 119(3), 1765–1790.
- Dinniman, M. S., Klinck, J. M., & Smith Jr, W. O. (2007). Influence of sea ice cover and icebergs on circulation and water mass formation in a numerical circulation model of the Ross Sea, Antarctica. *J. Geophys. Res.*, 112(C11).
- Fer, I., Voet, G., Seim, K. S., Rudels, B., & Latarius, K. (2010). Intense mixing of the Faroe Bank Channel overflow. *Geophys. Res. Lett.*, 37(2).
- Goldberg, D., Holland, D. M., & Schoof, C. (2009). Grounding line movement

- 1142 and ice shelf buttressing in marine ice sheets. *J. Geophys. Res.*, *114*, F04026,
1143 doi:10.1029/2008JF001227.
- 1144 Gräwe, U., Holtermann, P., Klingbeil, K., & Burchard, H. (2015). Advantages of
1145 vertically adaptive coordinates in numerical models of stratified shelf seas.
1146 *Ocean Modell.*, *92*, 56–68.
- 1147 Gwyther, D. E., Kusahara, K., Asay-Davis, X. S., Dinniman, M. S., & Galton-Fenzi,
1148 B. K. (2020). Vertical processes and resolution impact ice shelf basal melting:
1149 A multi-model study. *Ocean Modell.*, *147*, 101569.
- 1150 Haney, R. L. (1991). On the pressure gradient force over steep topography in sigma
1151 coordinate ocean models. *J. Phys. Oceanogr.*, *21*(4), 610–619.
- 1152 Hellmer, H. H., & Olbers, D. J. (1989). A two-dimensional model for the thermoha-
1153 line circulation under an ice shelf. *Antarctic Sci.*, *1*(4), 325–336.
- 1154 Hewitt, I. J. (2020). Subglacial plumes. *Ann. Rev. Fluid Mech.*, *52*, 145–169.
- 1155 Hofmeister, R., Burchard, H., & Beckers, J.-M. (2010). Non-uniform adaptive verti-
1156 cal grids for 3D numerical ocean models. *Ocean Modell.*, *33*(1-2), 70–86.
- 1157 Holland, D. M., & Jenkins, A. (1999). Modeling thermodynamic ice–ocean interac-
1158 tions at the base of an ice shelf. *J. Phys. Oceanogr.*, *29*(8), 1787–1800.
- 1159 Holland, P. R., & Feltham, D. L. (2006). The effects of rotation and ice shelf topog-
1160 raphy on frazil-laden ice shelf water plumes. *J. Phys. Oceanogr.*, *36*(12), 2312–
1161 2327.
- 1162 Jackett, D. R., McDougall, T. J., Feistel, R., Wright, D. G., & Griffies, S. M. (2006).
1163 Algorithms for density, potential temperature, conservative temperature, and
1164 the freezing temperature of seawater. *J. Atmos. Ocean. Tech.*, *23*(12), 1709–
1165 1728.
- 1166 Jenkins, A. (1991). A one-dimensional model of ice shelf-ocean interaction. *J. Geo-
1167 phys. Res.*, *96*(C11), 20671–20677.
- 1168 Jenkins, A. (1992). *Dynamics of Ronne ice shelf and its interaction with the ocean*
1169 (Unpublished doctoral dissertation). British Antarctic Survey, Natural Envi-
1170 ronment Research Council, Cambridge, England.
- 1171 Jenkins, A. (2011). Convection-driven melting near the grounding lines of ice shelves
1172 and tidewater glaciers. *J. Phys. Oceanogr.*, *41*(12), 2279–2294.
- 1173 Jenkins, A. (2016). A simple model of the ice shelf–ocean boundary layer and cur-
1174 rent. *J. Phys. Oceanogr.*, *46*(6), 1785–1803.
- 1175 Jenkins, A. (2021). Shear, stability, and mixing within the ice shelf–ocean boundary
1176 current. *J. Phys. Oceanogr.*, *51*(7), 2129–2148.
- 1177 Jenkins, A., Hellmer, H. H., & Holland, D. M. (2001). The role of meltwater ad-
1178 vection in the formulation of conservative boundary conditions at an ice–ocean
1179 interface. *J. Phys. Oceanogr.*, *31*(1), 285–296.
- 1180 Jenkins, A., Nicholls, K. W., & Corr, H. F. (2010). Observation and parameteriza-
1181 tion of ablation at the base of Ronne Ice Shelf, Antarctica. *J. Phys. Oceanogr.*,
1182 *40*(10), 2298–2312.
- 1183 Jungclauss, J. H., & Backhaus, J. O. (1994). Application of a transient reduced grav-
1184 ity plume model to the Denmark Strait Overflow. *J. Geophys. Res.*, *99*(C6),
1185 12375–12396.
- 1186 Kader, B. A. (1981). Temperature and concentration profiles in fully turbulent
1187 boundary layers. *Int. J. Heat Mass Transfer*, *24*(9), 1541–1544.
- 1188 Kader, B. A., & Yaglom, A. M. (1972). Heat and mass transfer laws for fully turbu-
1189 lent wall flows. *Int. J. Heat Mass Transfer*, *15*(12), 2329–2351.
- 1190 Klingbeil, K., Lemarié, F., Debreu, L., & Burchard, H. (2018). The numerics of
1191 hydrostatic structured-grid coastal ocean models: State of the art and future
1192 perspectives. *Ocean Modell.*, *125*, 80–105.
- 1193 Kochergin, V. P. (1987). Three-dimensional prognostic models. In N. S. Heaps (Ed.),
1194 *Three-dimensional coastal ocean models* (Vol. 4, pp. 201–208). Wiley Online Li-
1195 brary.
- 1196 Lange, X., & Burchard, H. (2019). The relative importance of wind straining and

- gravitational forcing in driving exchange flows in tidally energetic estuaries. *J. Phys. Oceanogr.*, *49*(3), 723–736.
- Li, Q., Bruggeman, J., Burchard, H., Klingbeil, K., Umlauf, L., & Bolding, K. (2021). Integrating CVMix into GOTM (v6. 0): A consistent framework for testing, comparing, and applying ocean mixing schemes. *Geosci. Model Dev.*, *14*, 4261–4282.
- Losch, M. (2008). Modeling ice shelf cavities in a z coordinate ocean general circulation model. *J. Geophys. Res.*, *113*, C08043, doi:10.1029/2007JC004368.
- Mayer, C., Schaffer, J., Hattermann, T., Floricioiu, D., Krieger, L., Dodd, P. A., ... Schannwell, C. (2018). Large ice loss variability at Nioghalvfjærdsfjorden glacier, northeast-greenland. *Nature*, *9*(1), 1–11.
- Mellor, G. L., McPhee, M. G., & Steele, M. (1986). Ice-seawater turbulent boundary layer interaction with melting or freezing. *J. Phys. Oceanogr.*, *16*(11), 1829–1846.
- Münchow, A., Padman, L., & Fricker, H. A. (2014). Interannual changes of the floating ice shelf of Petermann Gletscher, North Greenland, from 2000 to 2012. *J. Glaciol.*, *60*(221), 489–499.
- Omstedt, A., & Svensson, U. (1984). Modeling supercooling and ice formation in a turbulent Ekman layer. *J. Geophys. Res.*, *89*(C1), 735–744.
- Payne, A. J., Holland, P. R., Shepherd, A. P., Rutt, I. C., Jenkins, A., & Joughin, I. (2007). Numerical modeling of ocean-ice interactions under Pine Island Bay’s ice shelf. *J. Geophys. Res.*, *112*(C10).
- Rignot, E., & Steffen, K. (2008). Channelized bottom melting and stability of floating ice shelves. *Geophys. Res. Lett.*, *35*(2).
- Rosevear, M. G., Gayen, B., & Galton-Fenzi, B. K. (2021). The role of double-diffusive convection in basal melting of antarctic ice shelves. *Proc. Nat. Acad. Sci.*, *118*(6).
- Schaffer, J., Kanzow, T., von Appen, W.-J., von Albedyll, L., Arndt, J. E., & Roberts, D. H. (2020). Bathymetry constrains ocean heat supply to Greenland’s largest glacier tongue. *Nature Geosci.*, *13*(3), 227–231.
- Steele, M., Mellor, G. L., & McPhee, M. G. (1989). Role of the molecular sublayer in the melting or freezing of sea ice. *J. Phys. Oceanogr.*, *19*(1), 139–147.
- Straneo, F., & Cenedese, C. (2015). The dynamics of Greenland’s glacial fjords and their role in climate. *Annu. Rev. Mar. Sci.*, *7*, 89–112.
- Timmermann, R., Wang, Q., & Hellmer, H. (2012). Ice-shelf basal melting in a global finite-element sea-ice/ice-shelf/ocean model. *Annals Glaciology*, *53*(60), 303–314.
- Umlauf, L. (2009). The description of mixing in stratified layers without shear in large-scale ocean models. *J. Phys. Oceanogr.*, *39*(11), 3032–3039.
- Umlauf, L., & Arneborg, L. (2009). Dynamics of rotating shallow gravity currents passing through a channel. part i: Observation of transverse structure. *J. Phys. Oceanogr.*, *39*(10), 2385–2401.
- Umlauf, L., Arneborg, L., Burchard, H., Fiekas, V., Lass, H., Mohrholz, V., & Prandke, H. (2007). Transverse structure of turbulence in a rotating gravity current. *Geophys. Res. Lett.*, *34*(8).
- Umlauf, L., Arneborg, L., Hofmeister, R., & Burchard, H. (2010). Entrainment in shallow rotating gravity currents: A modeling study. *J. Phys. Oceanogr.*, *40*(8), 1819–1834.
- Umlauf, L., & Burchard, H. (2005). Second-order turbulence closure models for geophysical boundary layers. A review of recent work. *Conti. Shelf Res.*, *25*(7-8), 795–827.
- Vreugdenhil, C. A., & Taylor, J. R. (2019). Stratification effects in the turbulent boundary layer beneath a melting ice shelf: Insights from resolved large-eddy simulations. *J. Phys. Oceanogr.*, *49*(7), 1905–1925.
- Washam, P., Nicholls, K. W., Münchow, A., & Padman, L. (2020). Tidal modula-

- 1252 tion of buoyant flow and basal melt beneath Petermann Gletscher Ice Shelf,
1253 Greenland. *J. Geophys. Res.*, *125*(10), e2020JC016427.
- 1254 Wells, M., Cenedese, C., & Caulfield, C. (2010). The relationship between flux co-
1255 efficient and entrainment ratio in density currents. *J. Phys. Oceanogr.*, *40*(12),
1256 2713–2727.
- 1257 Yaglom, A. M., & Kader, B. A. (1974). Heat and mass transfer between a rough
1258 wall and turbulent fluid flow at high Reynolds and Peclet numbers. *J. Fluid*
1259 *Mech.*, *62*(3), 601–623.